1  **A hyper-immunogenic and slow-growing fungal strain induces a murine**

2  **granulomatous response to cryptococcal infection**

3

4  Running title: A murine cryptococcal granuloma model

5

6  Calla L. Telzrow,[a,b] Shannon Esher Righi,[c] Natalia Castro-Lopez,[d,e#] Althea

7  Campuzano,[d] Jacob T. Brooks,[f] John M. Carney,[a,g] Floyd L. Wormley Jr.,[d,e#] J. Andrew

8  Alspaugh[a,b]*

9

10  [a]Department of Medicine, Duke University School of Medicine, Durham, NC

11  [b]Department of Molecular Genetics and Microbiology, Duke University School of

12  Medicine, Durham, NC

13  [c]Department of Microbiology and Immunology, Tulane University School of Medicine,

14  New Orleans, LA

15  [d]Department of Biology, University of Texas at San Antonio, San Antonio, TX

16  [e]Department of Biology, Texas Christian University, Fort Worth, TX

17  [f]Department of Physics and Astronomy, University of North Carolina at Chapel Hill,

18  Chapel Hill, NC

19  [g]Department of Pathology, Duke University School of Medicine, Durham, NC

20

21  [#]Current address: Department of Biology, Texas Christian University, Fort Worth, TX

22

23

24    *Corresponding author:

25     J. Andrew Alspaugh

26    337 Sands Research Building

27    303 Research Drive, DUMC 102359

28    Durham, NC 27710, USA

29    Tel: (919) 684-0045

30    Fax: (919) 684-8902

31    andrew.alspaugh@duke.edu

32

33    Keywords: *Cryptococcus neoformans*, granuloma, GM-CSF, cell wall, Titan cell, cell

34    cycle defects, hypoxia

**ABSTRACT**

Many successful pathogens cause latent infections, remaining dormant within the host for years but retaining the ability to reactivate to cause symptomatic disease. The human opportunistic pathogen *Cryptococcus neoformans* is a ubiquitous yeast that establishes latent pulmonary infections in immunocompetent individuals upon fungal inhalation from the environment. These latent infections are frequently characterized by granulomas, or foci of chronic inflammation, that contain dormant cryptococcal cells. Immunosuppression causes these granulomas to break down and release viable fungal cells that proliferate, disseminate, and eventually cause lethal cryptococcosis. This course of *C. neoformans* dormancy and reactivation is understudied due to limited models, as chronic pulmonary granulomas do not typically form in most mouse models of cryptococcal infection. Here, we report that a previously characterized *Cryptococcus*-specific gene which is required for host-induced cell wall remodeling, *MAR1,* inhibits murine granuloma formation. Specifically, the *mar1Δ* loss-of-function mutant strain induces mature pulmonary granulomas at sites of infection dormancy in mice. Our data suggest that the combination of reduced fungal burden and increased immunogenicity of the *mar1Δ* mutant strain stimulates a host immune response that contains viable fungi within granulomas. Furthermore, we find that the *mar1Δ* mutant strain has slow growth and hypoxia resistance phenotypes, which may enable fungal persistence within pulmonary granulomas. Together with the conventional primary murine infection model, latent murine infection models will advance our understanding of cryptococcal disease progression and define fungal features important for persistence in the human host.

58 **INTRODUCTION**

59        Granulomas are complex foci of chronic inflammation that form in response to

60 many stimuli, including microbial infections. A hallmark of indolent infections such as

61 tuberculosis disease, granulomas are often characterized by epithelioid macrophages,

62 multinucleated giant cells, and dormant and/or slowly proliferating microorganisms (1–

63 4). The traditional understanding of the granuloma considered it to be a host-directed

64 defense response that restricts microbial access to nutrients and oxygen, resulting in an

65 immune microenvironment that limits microbial proliferation and prevents dissemination

66 (3, 4). However, more recent work has demonstrated that granulomas are a dynamic

67 component of the complex host-microbial "arms race". In addition to serving as a host-

68 directed protection mechanism, microorganisms can exploit the granuloma as a micro-

69 niche for long-term survival in the host, where they remain shielded from immune

70 detection until microbial reactivation (3–5). Although most work on granulomas has

71 been conducted in the context of mycobacterial infections, many other infectious

72 microorganisms induce granuloma formation in the human lung (6).

73        The fungal pathogen *Cryptococcus neoformans* is a significant cause of

74 pneumonia and fatal meningoencephalitis in immunocompromised populations around

75 the world, resulting in more than 180,000 deaths annually (7). Primary infection occurs

76 upon inhalation of environmental *C. neoformans* cells and/or spores, often early in life

77 (4, 8). Immunocompetent hosts typically control the primary infection, with fungi

78 remaining dormant but viable within lung-associated granulomas (9). As a result,

79 immunocompetent hosts do not manifest infection-related symptoms with disease

80 during this stage of latency (10). However, this latent infection can reactivate when a

4

81    previously exposed individual becomes immunocompromised, especially in the setting

82    of CD4+ T cell functional deficiency due to HIV infection, organ transplantation, and

83    immunosenescence (2, 4, 7, 11). Breakdown of the cryptococcal granuloma structure

84    results in microbial proliferation and systemic dissemination, including to the central

85    nervous system.

86         The reactivation of fungal cells from granulomas is an understudied facet of

87    cryptococcal disease, largely due to limited reactivation models. Although the mouse is

88    the most well-characterized and commonly used animal model to study *Cryptococcus*-

89    host interactions, many murine models do not form sustained granulomas in response

90    to clinically relevant isolates of *C. neoformans* (12). As a result, most murine

91    experiments focus on primary cryptococcal infection and subsequent systemic

92    dissemination. To explore cryptococcal latency and reactivation, investigators have

93    adopted models of cryptococcosis in rabbits (13) and rats (14, 15) or employed less

94    virulent *C. neoformans* strains in mice (12, 16, 17). Recently, a novel latent model was

95    reported in which pulmonary granulomas form in mice in response to infection with the

96    *gcs1Δ* mutant cryptococcal strain lacking the glucosylceramide synthase (18–21).

97    Mimicking the typical course of human disease, *gcs1Δ* cells induce well-formed

98    granulomas in the lungs which contain dormant *gcs1Δ* cells that become reactivated

99    from granulomas and disseminate upon immunosuppression (22).

100         We recently reported the identification and characterization of the *C. neoformans*

101    *MAR1* gene that is required for cell surface remodeling in response to the host

102    environment (23). The *mar1Δ* loss-of-function mutant strain displays altered cell surface

103    features when exposed to physiological conditions, including decreased cell wall

5

104    glucans and mannans, increased exposure of cell wall chitin, and impaired

105    polysaccharide capsule attachment (23). The cell surface alterations of the *mar1Δ*

106    mutant strain result in enhanced macrophage activation *in vitro* and hypovirulence in a

107    murine inhalation model of cryptococcosis (23). We report here that this hyper-

108    immunogenic *mar1Δ* mutant strain induces pulmonary granulomas in mice, resulting in

109    a chronic and indolent infection. Furthermore, we describe both fungal and host factors

110    that contribute to this granuloma response. From the fungal perspective, the

111    combination of reduced fungal burden and hyper-immunogenicity of the *mar1Δ* mutant

112    strain stimulates a host immune response that contains *mar1Δ* mutant cells within well-

113    circumscribed granulomas. From the host perspective, we find that host GM-CSF

114    signaling, a known contributor to granuloma formation (17, 24–26), is required for the

115    formation of these granulomas. Finally, *in vitro* studies demonstrate that the *mar1Δ*

116    mutant strain has cell cycle defects that may contribute to a slow growth phenotype and

117    hypoxia resistance, two features which likely enable cryptococcal persistence within

118    pulmonary granulomas. Because *MAR1* is a *Cryptococcus*-specific gene, this model

119    represents a unique addition to the limited tools available to study the reactivation

120    model of cryptococcal disease.

121

122    **MATERIALS & METHODS**

123    **Strains, media, and growth conditions**

124          All strains used in this study were generated in the *C. neoformans* var. *grubii* H99

125    (*MATα*) (13) background and are included in Table 1. Strains were maintained on yeast

126    extract-peptone-dextrose (YPD) medium (1% yeast extract, 2% peptone, 2% dextrose,

6

127  and 2% agar for solid medium). Unless otherwise indicated, strains were incubated at

128  30°C.

**Histology analyses**

130     The murine inhalation model of cryptococcosis was exclusively used in this study

131  (27). For initial histological examination, C57BL/6 female mice were acquired from

132  Charles River Laboratories. Mice were anesthetized with 2% isoflurane utilizing a rodent

133  anesthesia device (Eagle Eye Anesthesia, Jacksonville, FL) and were infected via the

134  intranasal route with 1 x $10^4$ CFU of either the wild-type (WT) (H99) or the *mar1Δ*

135  mutant (MAK1) strain. Mice were sacrificed at predetermined endpoints (3, 7, 14, and

136  40 DPI) by $CO_2$ inhalation followed by an approved secondary method of euthanasia.

137  Lungs were perfused with and stored in 10% neutral buffered formalin. Lungs were

138  subsequently paraffin-embedded, sectioned, mounted, and stained with hematoxylin

139  and eosin by the Duke University School of Medicine Research Immunohistochemistry

140  Shared Resource.

141     To determine the role of GM-CSF signaling in granuloma formation in this model,

142  lungs from male and female Csf2rb$^{-/-}$ mice (The Jackson Laboratory # 005940) were

143  prepared as described above, with a few alterations. Mice were sacrificed at the

144  predetermined endpoints of 3, 7, and 14 DPI by $CO_2$ inhalation followed by an approved

145  secondary method of euthanasia and lungs were perfused with PBS. The right lung was

146  stored in 10% neutral buffered formalin for future histopathology preparation, while the

147  left lung was used for fungal burden quantification analyses, as described below.

**Fungal burden quantification**

7

149    Mice were infected as described above. Mice were euthanized at predetermined

150    endpoints by $CO_2$ inhalation followed by cervical dislocation, and lung tissues and/or

151    brain tissues were excised. The left lobe of the lung and/or the brain was removed and

152    homogenized in 1 mL of sterile PBS as previously described (28) followed by culture of

153    10-fold dilutions of each homogenate on YPD agar medium supplemented with

154    chloramphenicol. Colony-forming units (CFU) were enumerated following incubation at

155    30°C for 48 hours. Statistical significance was determined using Student's *t* test

156    (GraphPad Software, San Diego, CA).

**Pulmonary cytokine analyses**

158    C57BL/6 female mice acquired from Charles River Laboratories were infected

159    and sacrificed as described above. Cytokine levels within the lung homogenates of

160    infected mice were analyzed using the Bio-Plex protein array system (Luminex-based

161    technology, Bio-Rad Laboratories, Hercules, CA). Briefly, lung tissues were excised and

162    homogenized in 1 mL ice-cold sterile PBS. An aliquot (50 µl) was taken to quantify the

163    pulmonary fungal burden, and an anti-protease buffer solution (1 mL) containing PBS,

164    protease inhibitors, and 0.05% Triton X-100 was added to the homogenate. Samples

165    were then clarified by centrifugation (3,500 rpm) for 10 minutes. Supernatants from

166    pulmonary homogenates were assayed for the presence of IL-1α, IL-1β, IL-2, IL-3, IL-4,

167    IL-5, IL-6, IL-9, IL-10, IL-12 (p40), IL-12 (p70), IL-13, IL-17, KC (CXCL1), MCP-1

168    (CCL2), MIP-1α (CCL3), MIP-1β (CCL4), RANTES (CCL5), Eotaxin (CCL11), IFN-γ,

169    tumor necrosis factor (TNF)-α, granulocyte macrophage-colony stimulating factor (GM-

170    CSF), and granulocyte-colony stimulating factor (G-CSF) according to the

171     manufacturer's instructions. Statistical significance between strains at each timepoint

172     was determined using Student's $t$ test (GraphPad Software, San Diego, CA).

173     **Pulmonary leukocyte isolation**

174          C57BL/6 female mice acquired from Charles River Laboratories were infected

175     and sacrificed as described above. Lungs of infected mice were excised on 1, 3, 7, 14,

176     and 21 DPI as previously described (28). Lungs were then digested enzymatically at

177     37°C for 30 minutes in 10 mL digestion buffer (RPMI 1640 and 1 mg/mL collagenase

178     type IV [Sigma-Aldrich, St. Louis, MO]) with intermittent (every 10 minutes) stomacher

179     homogenizations. The digested tissues were then successively filtered through sterile

180     70- and 40-µm nylon filters (BD Biosciences, San Diego, CA) to enrich for leukocytes,

181     and the cells were then washed three times with sterile Hank's Balanced Salt Solution

182     (HBSS). Erythrocytes were lysed by incubation in $NH_4Cl$ buffer (0.859% $NH_4Cl$, 0.1%

183     $KHCO_3$, 0.0372% $Na_2EDTA$ [pH 7.4]; Sigma-Aldrich) for 3 minutes on ice followed by a

184     2-fold excess of sterile PBS.

185     **Flow cytometry analyses**

186          Pulmonary leukocytes were isolated from infected mice as described above.

187     Standard methodology was employed for the direct immunofluorescence of pulmonary

188     leukocytes (28, 29). Briefly, in 96-well U-bottom plates, 100 µl containing $1 \times 10^6$ cells in

189     PBS were incubated with yellow Zombie viability dye (1:1000 dilution, Cat. No 423104,

190     Biolegend, San Diego, CA) for 15 minutes at room temperature followed by washing in

191     FACS buffer. Cells were then incubated with Fc block (1:500 dilution, Cat. # 553142,

192     clone 2.4G2, BD Biosciences) diluted in FACS buffer for 5 minutes to block nonspecific

193     binding of antibodies to cellular Fc receptors. Cells were then incubated with

9

194   fluorochrome-conjugated antibodies in various combinations to allow for multi-staining

195   for 30 minutes at 4°C. Cells were washed three times with FACS buffer and fixed in

196   200 μl of 2% ultrapure formaldehyde (Polysciences, Warrington, PA) diluted in FACS

197   buffer (fixation buffer). Fluorescence minus one (FMO) controls or cells incubated with

198   either FACS buffer alone, or single fluorochrome-conjugated antibodies were used to

199   determine positive staining and spillover/compensation calculations, and background

200   fluorescence was determined with FlowJo v.10.8 Software (FlowJo, LLC, Ashland, OR).

201   Raw data were collected with a Cell Analyzer LSRII (BD Biosciences) using BD

202   FACSDiva v8.0 software at the University of North Texas Health Sciences Center

203   (UNTHSC) Flow Core, and compensation and data analyses were performed using

204   FlowJo v.10.8 Software. Cells were first gated for lymphocytes (SSC-A vs. FSC-A) and

205   singlets (FSC-H vs. FSC-A). The singlets gate was further analyzed for the uptake of

206   live/dead yellow stain to determine live vs. dead cells. From live cells, cells were gated

207   on CD45+ cell expression. For data analyses, 100,000 events (cells) were evaluated

208   from a predominantly leukocyte population identified by back gating from CD45+ stained

209   cells. Statistical significance between strains at each timepoint was determined using

210   Student's *t* test (GraphPad Software, San Diego, CA).

211   **Macrophage activation analyses**

212        Intracellular staining of markers of macrophage activation was performed as

213   described previously (29). Leukocytes isolated from infected mice as described above

214   were incubated with cell stimulation cocktail (eBioscience Cat. # 00-4970-03) according

215   to the manufacturer's recommendation and incubated at 37°C in 5% $CO_2$ in cRPMI for

216   two hours in a six-well plate. Golgi plug (1:100 dilution, Brefeldin A, Cat. # 51-2301KZ,

217    BD Biosciences) was added according to the manufacturer's recommendations and

218    incubated for an additional four hours (6 hours total). Cells were washed with PBS and

219    stained with yellow Zombie viability dye in PBS at room temperature in the dark for

220    15 minutes. Cells were then washed with FACS buffer and incubated with Fc block (BD

221    Biosciences) diluted in FACS buffer for 5 minutes. For nitric oxide (iNOS) and Arginase

222    1 (Arg1) production in macrophages, cells were stained for surface markers CD45,

223    CD11b, CD64, F4/80, and CD24, and incubated at 4°C for 30 minutes. Cells were then

224    washed and fixed with 2% ultra-pure formaldehyde (Polysciences, Warrington, PA) for

225    20 minutes. Subsequently, cells were washed with 0.1% saponin buffer and stained with

226    antibodies for iNOS and Arg1 for 30 minutes at 4°C. Finally, cells were washed with

227    saponin buffer and fixed with 2% ultra-pure formaldehyde. Samples were processed

228    using a Cell Analyzer LSRII (BD Biosciences) using BD FACSDiva v8.0 software at the

229    UNTHSC Flow Core, and 100,000 events were collected for analysis using FlowJo

230    v.10.8 Software. Statistical significance between strains at each timepoint was

231    determined using Student's $t$ test (GraphPad Software, San Diego, CA).

232    **Titan cell assay and quantification**

233         A previously described *in vitro* titanization assay was used here (30). In brief, the

234    WT (H99), the *mar1Δ* mutant (MAK1), and the *mar1Δ + MAR1* (MAK11) strains were

235    incubated for 18 hours at 30°C, 150 rpm in 5 mL yeast nitrogen base (YNB) without

236    amino acids prepared according to the manufacturer's instructions plus 2% glucose.

237    Cultures were washed six times with PBS. An optical density at 600 nm ($OD_{600}$) of 0.001

238    for each strain was transferred to 5 mL 10% heat-inactivated fetal bovine serum (HI-

239    FBS) in PBS and incubated at 37°C, 5% $CO_2$ for 96 hours. Cells were imaged by

11

240 differential interference contrast (DIC) microscopy using a Zeiss Axio Imager A1

241 microscope equipped with an Axio-Cam MRm digital camera. Cell diameter was

242 measured using the ImageJ software (FIJI), and cells with a diameter > 10 μm were

243 considered Titan cells. A minimum of 400 cells were analyzed across three biological

244 replicates for each fungal strain. Statistical significance was determined using one-way

245 analysis of variance (ANOVA) and the Tukey-Kramer test (GraphPad Software, San

246 Diego, CA).

247 **SEM polysaccharide capsule visualization**

248 The WT (H99), the *mar1Δ* mutant (MAK1), the *mar1Δ + MAR1* (MAK11), and the

249 *cap59Δ* mutant (cap59) strains were incubated in YPD medium at 30°C and $CO_2$-

250 independent medium (Gibco) at 37°C until saturation. Samples were fixed with 2.5%

251 glutaraldehyde for 1 hour at room temperature and were subsequently washed 3 times

252 with PBS. Each sample was mounted onto 12 mm poly-L-lysine-coated coverslips

253 (Neuvitro Corporation) and subsequently dehydrated by immersing the coverslips in

254 ethanol (30% for 5 minutes, 50% for 5 minutes, 70% for 5 minutes, 95% for 10 minutes,

255 100% for 10 minutes, and 100% for 10 minutes). Samples were then critical point dried

256 with a Tousimis 931 critical point dryer (Rockville, Maryland) and coated with gold-

257 palladium using a Cressington 108 sputter-coater (Watford, United Kingdom).

258 Coverslips containing the prepared samples were mounted and imaged on a Hitachi S-

259 4700 scanning electron microscope (Tokyo, Japan).

260 **Cellular morphology defect quantification**

261 The WT (H99), the *mar1Δ* mutant (MAK1), and the *mar1Δ + MAR1* (MAK11)

262 strains were incubated for 18 hours in YPD medium at 30°C with shaking at 150 rpm. An

12

263    $OD_{600}$ of approximately 0.2 for each strain was transferred to fresh YPD medium and

264    subsequently incubated at either 30°C or 37°C for 18 hours with shaking at 150 rpm.

265    Cells were then pelleted, washed with PBS, and imaged by differential interference

266    contrast (DIC) microscopy. DIC images were captured using a Zeiss Axio Imager A1

267    microscope equipped with an Axio-Cam MRm digital camera. A minimum of 500 cells

268    were analyzed across three biological replicates for each strain using the ImageJ

269    software (FIJI). Statistical significance was determined using two-way analysis of

270    variance (ANOVA) and the Tukey-Kramer test (GraphPad Software, San Diego, CA).

271    **Growth curve analysis**

272        The WT (H99), the *mar1Δ* mutant (MAK1), and the *mar1Δ* + *MAR1* (MAK11)

273    strains were incubated for 18 hours in YPD medium at 30°C with 150 rpm shaking.

274    Cultures were normalized to an $OD_{600}$ of 0.01 in fresh YPD medium and added to wells

275    of a 96-well plate. Growth was then measured at an absorbance of 595 nm every 10

276    minutes for 40 hours with shaking between readings and incubation at 37°C. Control

277    wells containing YPD medium alone were also included to eliminate any background

278    absorbance.

279    **Hypoxia resistance analyses**

280        The WT (H99), the *mar1Δ* mutant (MAK1), the *mar1Δ* + *MAR1* (MAK11), and the

281    *sre1Δ* mutant (HEB6) strains were incubated in YPD medium at 30°C until mid-

282    logarithmic growth phase. Strains were washed once in PBS, normalized to an $OD_{600}$ of

283    0.6 in PBS, and serially diluted onto YES (0.5% [w/v] yeast extract, 2% glucose, and

284    225 µg/mL uracil, adenine, leucine, histidine, and lysine) medium agar plates with or

285    without cobalt chloride (0.7 mM) (31). Microaerophilic conditions were generated using

13

286 a sealed chamber (BD GasPak$^{TM}$) and two activated GasPak$^{TM}$ EZ Campy Container

287 System sachets (31). Plates were placed in the chamber (microaerophilic) or outside

288 the chamber (ambient air), incubated at 30°C, and imaged daily for 96 hours.

**Mouse isolate recovery and phenotypic characterization**

290 C57BL/6 female mice acquired from Charles River Laboratories were infected as

291 described above. At 61 DPI and 100 DPI, mice were sacrificed by $CO_2$ inhalation

292 followed by an approved secondary method of euthanasia and fungi were subsequently

293 isolated from the lungs as described above. Single fungal colonies were plated onto

294 YPD agar medium and subsequently frozen in separate wells of 96-well plates at -80°C.

295 Isolated fungi were stamped onto YPD agar medium incubated at 30°C, YPD agar

296 medium incubated at 37°C, YPD agar medium supplemented with nourseothricin (NAT)

297 (100 µg/mL) incubated at 30°C, and YPD agar medium buffered (150 mM HEPES) to

298 pH 8.15 incubated at 30°C. All plates were imaged daily. Mouse isolates were

299 determined to be *mar1Δ* mutant strain isolates based on growth on YPD + NAT medium

300 and dry colony morphology on YPD pH 8.15 medium (23). The original WT (H99) and

301 *mar1Δ* mutant (MAK1) strains were included on each plate as controls.

**Ethical use of animals**

303 All animal experiments in this manuscript were approved by the University of

304 Texas at San Antonio Institutional Animal Care and Use Committee (IACUC) (protocol

305 #MU021), the Texas Christian University and the University of North Texas Health

306 Sciences Center (UNTHSC) IACUC (protocol #1920-9), and the Duke University IACUC

307 (protocol #A102-20-05). Mice were handled according to IACUC guidelines.

**Data availability**

309     All fungal strains and reagents are available upon request.

310

311     **RESULTS**

312     **Pulmonary granulomas are formed and maintained in mice infected with the**

313     **_mar1Δ_ mutant strain.**

314           Based on our recent observations that the _mar1Δ_ mutant strain displays a highly

315     immunogenic cell surface, we hypothesized that the _mar1Δ_ mutant strain would have

316     unique interactions with the host _in vivo_. We previously observed that the _mar1Δ_ mutant

317     strain is hypovirulent compared to the wild-type (WT) strain in a murine inhalation model

318     of cryptococcosis (23). Highly immunogenic fungal strains often induce a

319     hyperinflammatory response that is detrimental to the host, resulting in hypervirulence

320     (32–34). We therefore explored in greater detail the mechanisms by which the highly

321     immunogenic _mar1Δ_ mutant strain simultaneously activates and is controlled by the

322     host immune response.

323           As an initial investigation into the interactions between the _mar1Δ_ mutant strain

324     and the host, we assessed the gross appearance of infected lungs from our previously

325     reported _mar1Δ_ mutant strain murine inhalation infection experiment. At the time of

326     sacrifice, generally between 24-40 days post-inoculation (DPI), we observed that the

327     lungs of _mar1Δ_-infected C57BL/6 mice displayed large, well-circumscribed inflammatory

328     foci surrounded by healthy-appearing lung tissue (Figure 1A). This contrasts starkly with

329     WT-infected lungs, which typically exhibit uncontrolled fungal proliferation accompanied

330     by a diffuse inflammatory response.

15

331    We examined histopathological features of infected murine lungs at specific

332    timepoints throughout the course of infection to further characterize the unique

333    pathology observed in *mar1Δ*-infected lungs. To do so, we replicated the experimental

334    approach used in Figure 1A; we inoculated C57BL/6 mice by inhalation with the WT

335    strain or the *mar1Δ* mutant strain and subsequently harvested lungs for analysis

336    throughout infection. At 3 DPI, an early timepoint in infection at which all inoculated

337    mice still appear healthy, the WT-infected and *mar1Δ*-infected lungs appear similar, with

338    the only notable exception being the increased number of fungal cells observed in the

339    WT-infected lungs (Figures 1B & S1). By 7 DPI, a timepoint in infection in which WT-

340    infected mice begin to show signs and symptoms of fungal disease but the *mar1Δ*-

341    infected mice still appear healthy, WT-infected lungs display numerous small foci of

342    inflammation (mean diameter = 535 μm) that contain some, but not all, fungal cells

343    (Figures 1B, 1C, & S1). As described previously, many of the WT fungal cells exhibit

344    signs of titanization (35). These foci of inflammation also occasionally display hallmarks

345    of early granuloma formation, such as the presence of epithelioid macrophages (1, 2, 4)

346    (Figure 1B). This type of immature granulomatous inflammatory response has been

347    reported previously in the C57BL/6 background infected with the *C. neoformans*

348    serotype D strain, 52D (17). In contrast, the *mar1Δ*-infected lungs have few visible

349    fungal cells and display a more uniform pattern of inflammation throughout the lungs at

350    7 DPI (Figures 1B). These observations demonstrate that distinct characteristics of the

351    *mar1Δ* mutant strain pathology emerge early in infection.

352    At 14 DPI, a timepoint in infection in which the WT-infected mice begin to

353    succumb to fungal infection and the *mar1Δ*-infected mice still appear healthy, WT cells,

354    many of which are titanized, proliferate throughout the lungs resulting in a scattered,

355    unorganized inflammatory response with mixed cell infiltrates (Figure 1B). Additionally,

356    most nascent granulomas have broken down, which may explain why this timepoint also

357    corresponds to a period of accelerating clinical symptoms and imminent mortality in WT-

358    infected mice (Figures 1B & 1C). In contrast, *mar1Δ*-infected lungs begin to form

359    granulomas by 14 DPI. Specifically, foci of inflammation appear (mean diameter = 866

360    μm), containing few fungal cells which are surrounded by regions of normal-appearing

361    lung tissue without fungal or inflammatory cells (Figures 1B & 1C). Additionally, these

362    inflammatory foci contain hallmarks of granulomas, such as epithelioid macrophages

363    surrounded by lymphocytes (1, 2, 4) (Figure 1B). In contrast to those infected with the

364    WT strain, the *mar1Δ*-infected mice display few infection-related symptoms at this

365    timepoint.

366        Many *mar1Δ*-infected mice survive to 40 DPI (23). At this late timepoint in

367    infection, mature granulomas are frequently observed (mean diameter = 1355 μm),

368    containing fungal cells, multinucleated giant cells, and palisading epithelioid

369    macrophages (Figures 1B, 1C, & S1). Additionally, no fungal cells are observed in lung

370    tissue outside of these granulomas. Collectively, these observations suggest differences

371    in the immune response in the context of WT and *mar1Δ* mutant strain infection. WT-

372    infected mice show a consistently robust mixed inflammatory response and variable

373    Titan cell response with vague granuloma formation during early stages of infection (7

374    DPI) (Figures 1B, 1C, & S1). This response is ineffective and is quickly overcome by

375    fungal growth, resulting in fungal proliferation throughout the lungs (14 DPI) (Figures 1B

376    & 1C). In contrast, the *mar1Δ*-infected mice show an absent to minimal inflammatory

17

377    response, absent Titan cell formation, and minimal granulomatous inflammatory

378    response during early stages of infection (7 DPI), with a more well-formed

379    granulomatous response in mice that survive to later timepoints in infection (40 DPI)

380    (Figures 1B, 1C, & S1). These *mar1Δ*-induced granulomas appear sufficient to contain

381    fungal proliferation.

382

383    **The *mar1Δ* mutant strain has a reduced fungal burden and hyper-immunogenicity**

384    ***in vivo.***

385        To explore possible mechanisms by which *mar1Δ* mutant strain infections induce

386    pulmonary granuloma formation, we assessed fungal burden and the pulmonary

387    immune response at timepoints relevant to granuloma formation. To do so, we

388    replicated the experimental approaches used in Figure 1; we inoculated C57BL/6 mice

389    by inhalation and harvested lungs for analysis throughout infection. We previously

390    reported a decrease in fungal burden in *mar1Δ*-infected lungs compared to WT-infected

391    lungs as early as 1 and 4 DPI, despite identical doses being used for both strains (23).

392    In this work, at all tested timepoints (3, 7, 14, & 21 DPI), we find that *mar1Δ*-infected

393    lungs have a significantly reduced fungal burden compared to WT-infected lungs.

394    Specifically, the *mar1Δ*-infected lungs have a 10-fold reduction in fungal burden at 3

395    DPI, a 100-fold reduction in fungal burden at 7 DPI, and a >500-fold reduction in fungal

396    burden at 14 and 21 DPI compared to WT-infected lungs (Figure 2). These observations

397    support the reduced number of *mar1Δ* mutant cells observed at these same timepoints

398    in our histopathology analyses (Figure 1B). As a result of the drastic reduction in

399    pulmonary fungal burden throughout infection, we observed that the *mar1Δ* mutant

400    strain rarely disseminates to the brain (Figure 2). When the *mar1Δ* mutant strain does

401    disseminate to the brain, the fungal burden is markedly lower than that of the WT strain

402    (Figure 2). Together, these observations indicate that the *mar1Δ* mutant strain has

403    reduced fungal burden in the murine lung and brain, reinforcing our previous reports

404    that the *mar1Δ* mutant strain has reduced fitness in host-relevant conditions.

405        Based on the drastic differences in fungal burden observed between WT-infected

406    and *mar1Δ*-infected lungs, we hypothesized that the immune microenvironment within

407    the lungs would also differ significantly. We replicated the experimental approaches

408    used in Figure 1; we inoculated C57BL/6 mice by inhalation and harvested lungs for

409    analysis throughout infection. At early timepoints in infection, 1 and 3 DPI, we observed

410    similar pulmonary cytokine profiles and leukocyte infiltrates within WT-infected lungs

411    and *mar1Δ*-infected lungs (Figures 3A, 3B, S2, & S3). The only significant difference

412    observed between the two infections was in the production of granulocyte macrophage-

413    colony stimulating factor (GM-CSF), a cytokine required for maturation of myeloid cells.

414    Specifically, *mar1Δ*-infected lungs display a significant increase in GM-CSF production

415    compared to WT-infected lungs at 3 DPI, an early timepoint in infection at which the

416    pulmonary immune response is being actively developed (Figures 3A & S2). Despite the

417    drastic reduction in *mar1Δ* mutant fungal burden at these early timepoints, the *mar1Δ*

418    mutant strain induces a cytokine and cellular response comparable to that of the WT

419    strain, likely due to the increased immunogenicity of the *mar1Δ* mutant cells.

420        As infection progressed to 7, 14, and 21 DPI, we observed marked reductions in

421    multiple cytokines (including IL-1β, IL-4, and GM-CSF) and leukocytes (including

422    CD45+ cells, alveolar macrophages [AM], and CD4+ T cells) in *mar1Δ*-infected lungs

423    compared to WT-infected lungs (Figures 3A, 3B, S2, & S3). These observations

424    demonstrate that by these timepoints in infection, the overall cytokine and cellular

425    response is reduced in *mar1Δ*-infected lungs compared to WT-infected lungs, likely due

426    to the sustained reduction in fungal burden present in the *mar1Δ*-infected lungs. This is

427    further supported by our histopathological observations made at the same timepoints

428    demonstrating more localized regions of inflammation in *mar1Δ*-infected lungs than in

429    WT-infected lungs (Figure 1B). We further explored macrophage polarization at these

430    same timepoints to determine whether the reduction in *mar1Δ* mutant strain fungal

431    burden, and the subsequent reduction in the pulmonary immune response, are due to

432    differences in macrophage activation (36). At each tested timepoint (7, 14, and 21 DPI),

433    we observed that the *mar1Δ*-infected lungs have a comparable number of or fewer

434    classically-activated (M1) and alternatively-activated (M2) alveolar and interstitial

435    macrophages compared to WT-infected lungs (Figure 3C). These observations

436    demonstrate that the *mar1Δ* mutant strain does not induce differential macrophage

437    polarization that results in a reduction in fungal burden and a more protective immune

438    response. Collectively, these data suggest that *mar1Δ*-induced pulmonary granuloma

439    formation appears to be a largely fungal-driven phenomenon. Despite reductions in

440    fungal burden, the *mar1Δ* mutant strain induces a WT strain-like immune response early

441    in infection that results in fungal containment within granulomas during mid-late stages

442    of infection. As infection matures and progresses, there is a marked decrease in many

443    cytokines and leukocytes infiltrating the *mar1Δ*-infected lung that corresponds with the

444    sustained reduction in fungal burden.

445

20

446 **Host GM-CSF signaling is required for pulmonary granuloma formation.**

447    Granuloma formation is dependent on GM-CSF signaling in the context of both

448    mycobacterial (24–26) and cryptococcal infections (17). GM-CSF is the only cytokine

449    that showed significant differential production in our cytokine analyses. Specifically, we

450    observed that the *mar1Δ* mutant strain induces more pulmonary GM-CSF production

451    than the WT strain at 3 DPI (Figures 3A & S2). We therefore hypothesized that GM-CSF

452    signaling would also be required for the formation of pulmonary granulomas in our

453    model. To test this hypothesis, we assessed the progression of infections with the WT

454    strain and the *mar1Δ* mutant strain in the Csf2rb$^{-/-}$ mouse background, which is defective

455    in GM-CSF signaling due to loss of the functional GM-CSF receptor. We inoculated

456    Csf2rb$^{-/-}$ mice using the inhalation route and harvested lungs for analysis throughout

457    infection. Overall, a similar pattern of inflammation was observed between mice infected

458    with the WT strain and mice infected with the *mar1Δ* mutant strain. We observed that

459    putative pulmonary granulomas are absent in Csf2rb$^{-/-}$ mice infected with either strain at

460    every tested timepoint (3, 7, and 14 DPI) (Figures 4A & S1). Instead, inflammation

461    appears unorganized and diffuse throughout the entirety of the lungs infected with either

462    fungal strain. Contrasting with the C57BL/6 infections, the Csf2rb$^{-/-}$ infections appear to

463    be characterized by fewer macrophages, which is expected based on previous work

464    that demonstrated that GM-CSF is required for macrophage recruitment to the lung

465    during early cryptococcal infection (17) (Figures 4A & S1). Like the C57BL/6 infections,

466    however, WT fungal cells are abundant throughout the lung, many with signs of

467    titanization, while *mar1Δ* mutant fungal cells are infrequently observed (Figures 4A &

468    S1). Pulmonary fungal burden assessed at 3 DPI confirms that *mar1Δ*-infected lungs

21

469    have a significantly lower fungal burden, with a 10-fold reduction compared to WT-

470    infected lungs, similar to what was observed in the C57BL/6 infections (Figure 4B).

471    These data demonstrate that GM-CSF signaling is required for granuloma formation in

472    both WT strain and *mar1Δ* mutant strain infections. However, because loss of GM-CSF

473    signaling does not rescue the reduction of *mar1Δ* mutant strain fungal burden during

474    early stages of infection, these data also suggest that GM-CSF signaling does not

475    exclusively drive the impaired fitness of *mar1Δ* mutant cells in the murine lung.

476

477    **The *mar1Δ* mutant strain is attenuated in the employment of various virulence**

478    **factors.**

479         In our fungal burden assays, we observed a modest increase in *mar1Δ* mutant

480    strain fungal burden as infection progressed from 3 to 21 DPI (Figure 2). Despite this,

481    we find that *mar1Δ*-infected mice can remain healthy-appearing and survive to at least

482    100 DPI. Furthermore, viable *mar1Δ* mutant cells that retain previously reported *mar1Δ*

483    mutant phenotypes, including dry colony morphology on alkaline pH and nourseothricin

484    (NAT) resistance (23), can be recovered from the lung at extended timepoints in

485    infection (61 and 100 DPI) (Figure S4). These observations indicate that the *mar1Δ*

486    mutant strain can persist within murine lung granulomas for extended periods of time

487    without causing any symptoms or signs of disease. Based on this observation, we

488    sought to understand the mechanism by which the *mar1Δ* mutant strain can survive and

489    persist in the mouse lung.

490         In both human and murine infections, a subset of cryptococcal cells form

491    enlarged Titan cells, an important virulence factor that enables cryptococcal persistence

22

492    in the lungs (35, 37). Using an established *in vitro* titanization assay (30), we observed

493    that the *mar1Δ* mutant strain is unable to form Titan cells (Figure 5A). This observation

494    supports our histopathology experiments, in which Titan cells were absent in *mar1Δ*-

495    infected lungs, collectively demonstrating that Titan cell formation does not explain the

496    persistence of *mar1Δ* mutant cells within granulomas.

497         We previously reported that the *mar1Δ* mutant strain is impaired in the

498    implementation of the polysaccharide capsule, assessed by India ink staining (23). We

499    utilized high-resolution scanning electron microscopy (SEM) to more rigorously study

500    the *mar1Δ* mutant strain capsule architecture. In permissive growth conditions (YPD

501    medium, 30°C), the capsule of the *mar1Δ* mutant strain is nearly indistinguishable from

502    that of the WT strain, which contrasts starkly with the acapsular *cap59Δ* mutant strain

503    (Figure 5B). However, in capsule-inducing conditions (TC medium, 37°C), the *mar1Δ*

504    mutant strain lacks the degree of capsule fiber elongation observed in the WT strain,

505    explaining the reduction in India ink exclusion previously reported for the *mar1Δ* mutant

506    strain (23) (Figure 5B). The inability of the *mar1Δ* mutant strain to employ these two

507    important virulence factors, Titan cells and polysaccharide capsule, likely drive the

508    hyper-immunogenicity observed in our murine infection studies.

509

510    **The *mar1Δ* mutant strain displays cell cycle defects that result in a slow growth**

511    **phenotype and hypoxia resistance.**

512         Both Titan cell formation (30, 38) and polysaccharide capsule elaboration (39–

513    41) are known to be mediated by the cell cycle, suggesting that the *mar1Δ* mutant strain

514    may be unable to properly employ these virulence factors due to defects in cell cycle

515    progression. To explore cell cycle progression in the *mar1Δ* mutant strain background,

516    we observed *mar1Δ* mutant cell morphology during logarithmic growth phase. When

517    incubated at the permissive temperature of 30°C, the *mar1Δ* mutant strain displays an

518    increased incidence of cytokinesis defects (such as elongated cells, cells with wide bud

519    necks, and cells that fail to complete cytokinesis), compared to both the WT strain and

520    the *mar1Δ* + *MAR1* complemented strain (Figure 6A). The frequency of these

521    cytokinesis defects is significantly enhanced at the physiological temperature of 37°C

522    (Figure 6A). We next determined the impact of these defects on the growth kinetics of

523    the *mar1Δ* mutant strain. We observed that the *mar1Δ* mutant strain displays a

524    reduction in growth during logarithmic phase at 37°C, compared to both the WT strain

525    and the *mar1Δ* + *MAR1* complemented strain (Figure 6B). These data demonstrate that

526    the *mar1Δ* mutant strain has a slow growth phenotype at the physiological temperature

527    of 37°C that is likely driven in part by cytokinesis defects.

528         Cell cycle regulation is also known to be related to fungal adaptation to hypoxia

529    (42–44). Because *C. neoformans* is an obligate aerobe, WT fungal cells undergo $G_2$-

530    arrest in response to hypoxia (45, 46). We assessed the ability of the *mar1Δ* mutant

531    strain to grow in an environment with reduced oxygen availability by observing growth in

532    the presence of $CoCl_2$ and in a microaerophilic chamber. In both cases, we observed

533    that the *mar1Δ* mutant strain displays enhanced growth compared to the WT strain and

534    the *mar1Δ* + *MAR1* complemented strain (Figure 6C). In these assays, the $CoCl_2$- and

535    hypoxia-sensitive *sre1Δ* mutant strain was used as a control (31) (Figure 6C).

536    Collectively, these observations suggest that the cell cycle defects of the *mar1Δ* mutant

24

537    strain may contribute to its ability to survive, slowly proliferate, and persist in the murine

538    granuloma environment.

539

540    **DISCUSSION**

541         Here, we report and characterize the host response to a chronic and indolent *C.*

542    *neoformans* lung infection, one distinguished by sustained granulomas. Using the

543    inhalation route of infection in C57BL/6 mice, we observe granuloma formation in

544    infections due to both the WT and *mar1Δ* mutant strains. However, the appearance,

545    development, and maintenance of these granulomas differ significantly. In WT

546    infections, small, immature granulomas form early in infection. As infection progresses,

547    these nascent granulomas begin to degenerate, leading to fungal proliferation

548    throughout the lungs, fungal dissemination to the brain, and eventually murine death.

549    This type of early, immature granuloma formation has been observed previously in

550    murine infections with other *C. neoformans* WT strains (16, 17). In contrast, in *mar1Δ*

551    mutant strain infections we observe mature pulmonary granulomas that develop over

552    several weeks in the absence of overt clinical symptoms. These granulomas differ from

553    the WT-induced granulomas because they appear later in infection, are typically larger,

554    and are more contained. The containment of these granulomas may be expected

555    because *mar1Δ*-induced granulomas are associated with a significantly lower fungal

556    burden compared to WT strain infections, suggesting that the granulomas effectively

557    inhibit fungal proliferation throughout the lungs. Despite this drastic reduction in fungal

558    burden, the *mar1Δ* mutant strain induces a comparable pulmonary cytokine and

559    leukocyte response to that of the WT strain during early stages of infection. Previous

560   work reported by our group characterized the *mar1Δ* mutant strain as more

561   immunogenic than the WT strain, due to its poorly organized cell wall and impaired

562   polysaccharide capsule attachment (23). We posit that the combination of reduced

563   fungal burden and increased immunogenicity drives *mar1Δ*-induced granuloma

564   formation: the increased immunogenicity results in an immune response that contains

565   the reduced number of *mar1Δ* mutant cells within granulomas during early stages in

566   infection.

567      We further observe that *mar1Δ*-induced granulomas are maintained throughout

568   infection, from 14 DPI to as late as 100 DPI. We find that the immune microenvironment

569   associated with these granulomas has significantly reduced cytokine and leukocyte

570   responses. Previous work has implicated classically-activated macrophage polarization

571   in enhanced antifungal activity of macrophages (47–49). We find that *mar1Δ*-infected

572   lungs have a comparable number of or fewer (depending on the timepoint) classically-

573   activated (M1) and alternatively-activated (M2) macrophages compared to WT-infected

574   lungs, suggesting that differential polarization of macrophages does not contribute to

575   the reduced fungal burden and associated immune response in *mar1Δ*-infected lungs.

576   Collectively, these observations demonstrate that *mar1Δ*-induced granulomas are

577   largely a fungal-driven phenomenon, with the sustained reduction in *mar1Δ* mutant

578   strain fungal burden resulting in a dampened immune response compared with WT-

579   infected lungs. Using these approaches, we have defined a detailed timeline of

580   granuloma formation, in both WT and *mar1Δ* mutant strain infections, and characterized

581   multiple fungal factors that contribute to granuloma formation (Figure S5).

582     In addition to the fungal drivers of *mar1Δ*-induced granuloma formation described

583     above, we have also confirmed the role of GM-CSF as a host driver of cryptococcal

584     granuloma formation. From our pulmonary cytokine analyses, we observed that GM-

585     CSF is the only differentially produced cytokine in *mar1Δ*-infected lungs compared to

586     WT-infected lungs. Specifically, GM-CSF is elevated in *mar1Δ*-infected lungs at 3 DPI,

587     an early timepoint in infection at which the pulmonary immune response is being

588     actively developed. This increased GM-CSF production may be a result of increased

589     Dectin-1 activation by the *mar1Δ* mutant strain. We previously reported that the *mar1Δ*

590     mutant strain is partially recognized by the pathogen recognition receptor Dectin-1,

591     likely due its increased exposed surface β-glucan and chitin (23). Dectin-1 has been

592     shown to be required for normal GM-CSF production in murine macrophages (50).

593     Additionally, GM-CSF production is known to result in an increase in Dectin-1

594     expression by murine macrophages (50, 51). We also report that granuloma formation

595     is dependent on GM-CSF signaling, as granulomas are absent in Csf2rb$^{-/-}$ mouse

596     background infections with either the WT or *mar1Δ* mutant strains. These results are

597     expected because GM-CSF plays a significant role in both *C. gattii* and *C. neoformans*

598     infections, as individuals with GM-CSF autoantibodies are unusually susceptible to

599     cryptococcal infection (52–54). Furthermore, previous work in both mycobacterial (24–

600     26) and cryptococcal infections (17) has demonstrated that GM-CSF signaling is

601     required for granuloma formation, likely due to its requirement for macrophage

602     recruitment to the lung during early stages of infection. Our model enables further

603     exploration of the requirement of GM-CSF for granuloma maintenance. For example,

604     future experiments can introduce GM-CSF antibodies into *mar1Δ*-infected mice to

605    determine whether GM-CSF is required for *mar1Δ*-induced granuloma maintenance and

606    control of infection. Furthermore, WT strain infections can be supplemented with

607    exogenous GM-CSF to determine whether increased GM-CSF can help maintain WT-

608    induced granulomas.

609      Despite the reduced fungal burden of the *mar1Δ* mutant strain compared to the

610    WT strain, the *mar1Δ* mutant strain persists in the murine lung long-term, up to 100 DPI.

611    Titan cell formation is a well-characterized persistence mechanism that is specific to

612    *Cryptococcus* species (35, 37). Results from an established *in vitro* titanization assay

613    (30) in combination with our histopathological observations demonstrate that the *mar1Δ*

614    mutant strain is unable to form Titan cells, and as a result, Titan cells do not explain the

615    persistence of the *mar1Δ* mutant strain in the murine lung. We also observed that the

616    *mar1Δ* mutant strain is attenuated in the implementation of another important virulence

617    factor, the polysaccharide capsule. Although the *mar1Δ* mutant strain has a similar

618    basal level of capsule to the WT strain, it is unable to extend its capsule to the level of

619    the WT strain in response to capsule-inducing signals.

620      The expression of many virulence factors is known to be mediated by the cell

621    cycle (41). Furthermore, recent work has proposed that *C. neoformans* undergoes a

622    unique cell cycle *in vivo*, the "stress cell cycle", that regulates the employment of various

623    virulence factors (55). Titan cells are polyploid cryptococcal cells that form in both

624    human and mouse lungs during infection (35, 37). This polyploidization and concomitant

625    cell body enlargement is negatively regulated by the transcription factor Usv101, which

626    acts downstream of the cell cycle regulator Swi6 (30, 38). Furthermore, recent work has

627    found that the cyclin, Cln1, contributes to Titan cell formation by regulating DNA

628    replication and cell division after $G_2$-arrest *in vivo* (55). Similarly, capsule elongation is

629    also regulated by the cell cycle, with the majority of capsule elongation occurring in $G_1$

630    phase of the cell cycle (40). The dysregulation of these cell cycle-mediated virulence

631    factors suggests that the *mar1Δ* mutant strain harbors cell cycle defects.

632        We indeed observed that the *mar1Δ* mutant strain displays a marked increase in

633    cytokinesis defects compared to the WT strain, at both 30°C and 37°C, leading to a

634    decreased growth rate. In various cell types, including stem cells (56), tumor cells (57),

635    bacteria (58), and fungi (43), a reduction in growth rate is required for survival in the

636    presence of hypoxia. It is possible that its inherent decreased growth rate predisposes

637    the *mar1Δ* mutant strain to growth in a hypoxic environment. The mammalian

638    environment is known to limit oxygen availability to invading microorganisms, as a

639    stressor used to contain microbial proliferation (42). This important resource is likely

640    even further restricted within the pulmonary granuloma, which is known to have

641    suboptimal oxygen levels in the context of mycobacterial infection (59). Recent work by

642    the Alanio laboratory has demonstrated that cryptococcal dormancy can be induced by

643    a combination of nutrient and oxygen deprivation (44, 60). Furthermore, the Dromer

644    laboratory has found that dormant cryptococcal cells are characterized by reduced

645    metabolic activity and delayed growth (43). With these observations in mind, it is

646    possible that the slow growth and hypoxia resistance phenotypes of the *mar1Δ* mutant

647    strain enable its survival and persistence within granulomas in the model described

648    here. Further work will be required to determine whether these phenotypes are

649    necessary and/or sufficient for fungal survival and persistence within granulomas.

650    The Del Poeta laboratory has developed the most well-characterized murine

651    pulmonary granuloma model of cryptococcal disease to date using the *gcs1Δ* mutant

652    strain. From the fungal perspective, the *gcs1Δ* mutant strain lacks the membrane

653    sphingolipid glucosylceramide, making it an obligate intracellular pathogen and, as a

654    result, completely avirulent in a murine inhalation model, the route of infection that most

655    closely replicates the course of human infection (18, 19). It is noteworthy that both the

656    *gcs1Δ* mutant strain and the *mar1Δ* mutant strain are constructed in the same WT strain

657    background, and as a result, these two mutant strains are comparable and can

658    potentially be used together to explore the complex characteristics of granuloma

659    formation. For example, both strains display cell cycle defects in the presence of

660    physiological stress: the *gcs1Δ* mutant strain arrests at alkaline pH (18) and the *mar1Δ*

661    mutant strain displays cytokinesis defects at 37°C. These similarities suggest that a

662    slow growth phenotype in the host environment may favor fungal containment with

663    granulomas. Virulence potential is a notable difference between the strains. The *gcs1Δ*

664    mutant strain is unable to initiate infection and disease via the inhalation route of

665    infection (18), categorizing *GCS1* as a disease initiation factor (61). In contrast, the

666    *mar1Δ* mutant strain can establish infection and cause fatal disease in nearly half of the

667    infected mice (23), making *MAR1* a disease progression factor (61). This may be

668    related to the fact that *GCS1* orthologs are found in many pathogenic fungi (18), while

669    *MAR1* appears to be a *Cryptococcus*-specific gene (23). These contrasting features

670    suggest that granuloma formation is a highly complex process that relies on the

671    interplay between many fungal and host factors.

672    From the host perspective, *gcs1Δ*-induced granuloma formation requires host

673    sphingosine kinase 1-sphingosine 1-phosphate (SK1-S1P) signaling (20, 21). Most

674    recently, the Del Poeta laboratory has applied this model to explore cryptococcal

675    reactivation. Mimicking human disease, *gcs1Δ* mutant cells become reactivated from

676    granulomas and disseminate upon immunosuppression with the multiple sclerosis

677    therapeutic FTY720, which suppresses SK1-S1P signaling (22). This model has

678    enabled the first murine reactivation studies of cryptococcal infection. Future work with

679    *mar1Δ*-induced granulomas can similarly explore reactivation in the context of

680    immunosuppression, to better understand the typical course of cryptococcal disease in

681    humans. One of the populations most vulnerable to cryptococcal reactivation includes

682    untreated HIV/AIDS patients (7). In our leukocyte infiltrate analyses, we observed that

683    *mar1Δ*-infected lungs have an enhanced CD4+ T cell response compared to WT-

684    infected lungs at 21 DPI. This observation is particularly striking because *mar1Δ*-

685    infected lungs have a decreased or equivalent response compared to WT-infected lungs

686    for all other leukocytes tested at this same timepoint. CD4+ T cells are present in

687    pulmonary granulomas of immunocompetent individuals (62). Furthermore, CD4+ T

688    cells border the periphery of pulmonary granulomas in HIV+ individuals receiving

689    antiretroviral therapy, but they are lost in individuals with advanced HIV/AIDS,

690    suggesting that CD4+ lymphocytes may be involved in granuloma maintenance (2, 62).

691    By inducing CD4+ T cell depletion, and as a result mimicking the HIV/AIDS disease

692    state, we can probe the role of CD4+ T cells in the maintenance of granulomas in this

693    model. Following immunosuppression, we can observe *mar1Δ*-infected mice to track

694    granuloma breakdown and fungal proliferation with the same approaches used here.

695 Considering both the fungal and host drivers of granuloma formation outlined here, this

696 model harbors features that make it unique from other existing cryptococcal granuloma

697 models.

698

699 **ACKNOWLEDGEMENTS**

713

714 **CONFLICT OF INTEREST**

715 The authors declare there is no conflict of interest.

716

717 **REFERENCES**

718    1.    Adams DO. 1976. The granulomatous inflammatory response. A review. *Am J*

719         *Pathol* 84:164–191.

720    2.    Shibuya K, Hirata A, Omuta J, Sugamata M, Katori S, Saito N, Murata N, Morita

721         A, Takahashi K, Hasegawa C, Mitsuda A, Hatori T, Nonaka H. 2005. Granuloma

722         and cryptococcosis. *J Infect Chemother* 11:115–122.

723    3.    Ramakrishnan L. 2012. Revisiting the role of the granuloma in tuberculosis. *Nat*

724         *Rev Immunol* 12:352–366.

725    4.    Ristow LC, Davis JM. 2021. The granuloma in cryptococcal disease. *PLoS*

726         *Pathog* 17:e1009342.

727    5.    Oehlers SH, Cronan MR, Scott NR, Thomas MI, Okuda KS, Walton EM, Beerman

728         RW, Crosier PS, Tobin DM. 2015. Interception of host angiogenic signalling limits

729         mycobacterial growth. *Nature* 517:612–615.

730    6.    Zumla A, James DG. 1996. Granulomatous infections: etiology and classification.

731         *Clin Infect Dis* 23:146–158.

732    7.    Rajasingham R, Smith RM, Park BJ, Jarvis JN, Govender NP, Chiller TM,

733         Denning DW, Loyse A, Boulware DR. 2017. Global burden of disease of HIV-

734         associated cryptococcal meningitis: an updated analysis. *Lancet Infect Dis*

735         17:873–881.

736    8.    Goldman DL, Khine H, Abadi J, Lindenberg DJ, Priofski LA, Niang R, Casadevall

737         A. 2001. Serologic evidence for *Cryptococcus neoformans* infection in early

738         childhood. *Pediatrics* 107:E66.

739    9.    McDonnell JM, Hutchins GM. 1985. Pulmonary cryptococcosis. *Hum Pathol*

740         16:121–128.

741    10.    Warr W, Bates JH, Stone A. 1968. The spectrum of pulmonary cryptococcosis.

742           *Ann Intern Med* 69:1109–1116.

743    11.    Grebenciucova E, Reder AT, Bernard JT. 2016. Immunologic mechanisms of

744           fingolimod and the role of immunosenescence in the risk of cryptococcal infection:

745           a case report and review of literature. *Mult Scler Relat Disord* 9:158–162.

746    12.    Normile TG, Bryan AM, Poeta MD. 2020. Animal models of Cryptococcus

747           neoformans in identifying immune parameters associated with primary infection

748           and reactivation of latent infection. *Front Immunol* 11:581750.

749    13.    Perfect JR, Lang SD, Durack DT. 1980. Chronic cryptococcal meningitis: a new

750           experimental model in rabbits. *Am J Pathol* 101:177–194.

751    14.    Goldman D, Cho Y, Zhao M, Casadevall A, Lee SC. 1996. Expression of inducible

752           nitric oxide synthase in rat pulmonary *Cryptococcus neoformans* granulomas. *Am

753           J Pathol* 148:1275–1282.

754    15.    Kobayashi M, Ito M, Sano K, Koyama M. 2000. Granulomatous and cytokine

755           responses to pulmonary *Cryptococcus neoformans* in two strains of rats.

756           *Mycopathologia* 151:121–130.

757    16.    Feldmesser M, Casadevall A, Kress Y, Spira G, Orlofsky A. 1997. Eosinophil-

758           *Cryptococcus neoformans* interactions *in vivo* and *in vitro*. *Infect Immun* 65:1899–

759           1907.

760    17.    Chen GH, Olszewski MA, Mcdonald RA, Wells JC, Paine R, Huffnagle GB, Toews

761           GB. 2007. Role of granulocyte macrophage colony-stimulating factor in host

762           defense against pulmonary *Cryptococcus neoformans* infection during murine

763           allergic bronchopulmonary mycosis. *Am J Pathol* 170:1028–1040.

764    18.    Rittershaus PC, Kechichian TB, Allegood JC, Merrill AH, Hennig M, Luberto C,

765           Poeta MD. 2006. Glucosylceramide synthase is an essential regulator of

766           pathogenicity of *Cryptococcus neoformans*. *J Clin Invest* 116:1651–1659.

767    19.    Kechichian TB, Shea J, Poeta MD. 2007. Depletion of alveolar macrophages

768           decreases the dissemination of a glucosylceramide-deficient mutant of

769           *Cryptococcus neoformans* in immunodeficient mice. *Infect Immun* 75:4792–4798.

770    20.    McQuiston T, Luberto C, Poeta MD. 2010. Role of host sphingosine kinase 1 in

771           the lung response against cryptococcosis. *Infect Immun* 78:2342–2352.

772    21.    Farnoud AM, Bryan AM, Kechichian T, Luberto C, Poeta MD. 2015. The

773           granuloma response controlling cryptococcosis in mice depends on the

774           sphingosine kinase 1–sphingosine 1-phosphate pathway. *Infect Immun* 83:2705–

775           2713.

776    22.    Bryan AM, You JK, McQuiston T, Lazzarini C, Qiu Z, Sheridan B, Nuesslein-

777           Hildesheim B, Poeta MD. 2020. FTY720 reactivates cryptococcal granulomas in

778           mice through S1P receptor 3 on macrophages. *J Clin Invest* 130:4546–4560.

779    23.    Esher SK, Ost KS, Kohlbrenner MA, Pianalto KM, Telzrow CL, Campuzano A,

780           Nichols CB, Munro C, Wormley FL, Alspaugh JA. 2018. Defects in intracellular

781           trafficking of fungal cell wall synthases lead to aberrant host immune recognition.

782           *PLoS Pathog* 14:e1007126.

783    24.    Gonzalez-Juarrero M, Hattle JM, Izzo A, Junqueira-Kipnis AP, Shim TS, Trapnell

784           BC, Cooper AM, Orme IM. 2005. Disruption of granulocyte macrophage-colony

785           stimulating factor production in the lungs severely affects the ability of mice to

786           control *Mycobacterium tuberculosis* infection. *J Leukoc Biol* 77:914–922.

787    25.    Szeliga J, Daniel DS, Yang CH, Sever-Chroneos Z, Jagannath C, Chroneos ZC.

788           2008. Granulocyte-macrophage colony stimulating factor-mediated innate

789           responses in tuberculosis. *Tuberculosis* 88:7–20.

790    26.    Benmerzoug S, Marinho FV, Rose S, Mackowiak C, Gosset D, Sedda D, Poisson

791           E, Uyttenhove C, Van Snick J, Jacobs M, Garcia I, Ryffel B, Quesniaux VFJ.

792           2018. GM-CSF targeted immunomodulation affects host response to *M.*

793           *tuberculosis* infection. *Sci Rep* 8:8652.

794    27.    Cox GM, Mukherjee J, Cole GT, Casadevall A, Perfect JR. 2000. Urease as a

795           virulence factor in experimental cryptococcosis. *Infect Immun* 68:443–448.

796    28.    Leopold Wager C, Hole CR, Wozniak KL, Olszewski MA, Mueller M, Wormley FL.

797           2015. *STAT1* signaling within macrophages is required for antifungal activity

798           against *Cryptococcus neoformans*. *Infect Immun* 83:4513–4527.

799    29.    Hole CR, Leopold Wager CM, Castro-Lopez N, Campuzano A, Cai H, Wozniak

800           KL, Wang Y, Wormley FL. 2019. Induction of memory-like dendritic cell responses

801           *in vivo*. *Nat Commun* 10:2955.

802    30.    Dambuza IM, Drake T, Chapuis A, Zhou X, Correia J, Taylor-Smith L, LeGrave N,

803           Rasmussen T, Fisher MC, Bicanic T, Harrison TS, Jaspars M, May RC, Brown

804           GD, Yuecel R, MacCallum DM, Ballou ER. 2018. The *Cryptococcus neoformans*

805           Titan cell is an inducible and regulated morphotype underlying pathogenesis.

806           *PLoS Pathog* 14:e1006978.

807    31.    Brown HE, Telzrow CL, Saelens JW, Fernandes L, Alspaugh JA. 2020. Sterol-

808           response pathways mediate alkaline survival in diverse fungi. *mBio* 11:e00719-

809           20.

36

810   32.   Al-Bader N, Vanier G, Liu H, Gravelat FN, Urb M, Hoareau CMQ, Campoli P,

811          Chabot J, Filler SG, Sheppard DC. 2010. Role of trehalose biosynthesis in

812          *Aspergillus fumigatus* development, stress response, and virulence. *Infect Immun*

813          78:3007–3018.

814   33.   Ost KS, O'Meara TR, Huda N, Esher SK, Alspaugh JA. 2015. The *Cryptococcus*

815          *neoformans* alkaline response pathway: identification of a novel Rim pathway

816          activator. *PLoS Genet* 11:e1005159.

817   34.   Zacharias CA, Sheppard DC. 2019. The role of *Aspergillus fumigatus*

818          polysaccharides in host–pathogen interactions. *Curr Opin Microbiol* 52:20–26.

819   35.   Zaragoza O, García-Rodas R, Nosanchuk JD, Cuenca-Estrella M, Rodríguez-

820          Tudela JL, Casadevall A. 2010. Fungal cell gigantism during mammalian

821          infection. *PLoS Pathog* 6:e1000945.

822   36.   McQuiston TJ, Williamson PR. 2012. Paradoxical roles of alveolar macrophages

823          in the host response to *Cryptococcus neoformans*. *J Infect Chemother* 18:1–9.

824   37.   Cruickshank JG, Cavill R, Jelbert M. 1973. *Cryptococcus neoformans* of unusual

825          morphology. *Appl Microbiol* 25:309–312.

826   38.   Hommel B, Mukaremera L, Cordero RJB, Coelho C, Desjardins CA, Sturny-

827          Leclère A, Janbon G, Perfect JR, Fraser JA, Casadevall A, Cuomo CA, Dromer F,

828          Nielsen K, Alanio A. 2018. Titan cells formation in *Cryptococcus neoformans* is

829          finely tuned by environmental conditions and modulated by positive and negative

830          genetic regulators. *PLoS Pathog* 14:e1006982.

831   39.   Zaragoza O, Telzak A, Bryan RA, Dadachova E, Casadevall A. 2006. The

832          polysaccharide capsule of the pathogenic fungus *Cryptococcus neoformans*

833    enlarges by distal growth and is rearranged during budding. *Mol Microbiol* 59:67–

834    83.

835  40.  García-Rodas R, Cordero RJB, Trevijano-Contador N, Janbon G, Moyrand F,

836    Casadevall A, Zaragoza O. 2014. Capsule growth in *Cryptococcus neoformans* Is

837    coordinated with cell cycle progression. *mBio* 5:e00945-14.

838  41.  Kelliher CM, Leman AR, Sierra CS, Haase SB. 2016. Investigating conservation

839    of the cell-cycle-regulated transcriptional program in the fungal pathogen,

840    *Cryptococcus neoformans*. *PLoS Genet* 12:e1006453.

841  42.  Grahl N, Shepardson KM, Chung D, Cramer RA. 2012. Hypoxia and fungal

842    pathogenesis: to air or not to air? *Eukaryot Cell* 11:560–570.

843  43.  Alanio A, Vernel-Pauillac F, Sturny-Leclère A, Dromer F. 2015. *Cryptococcus*

844    *neoformans* host adaptation: toward biological evidence of dormancy. *mBio*

845    6:e02580-14.

846  44.  Hommel B, Sturny-Leclère A, Volant S, Veluppillai N, Duchateau M, Yu CH,

847    Hourdel V, Varet H, Matondo M, Perfect JR, Casadevall A, Dromer F, Alanio A.

848    2019. *Cryptococcus neoformans* resists to drastic conditions by switching to

849    viable but non-culturable cell phenotype. *PLoS Pathog* 15:e1007945.

850  45.  Ohkusu M, Raclavsky V, Takeo K. 2001. Deficit in oxygen causes $G_2$ budding and

851    unbudded $G_2$ arrest in *Cryptococcus neoformans*. *FEMS Microbiol Lett* 204:29–

852    32.

853  46.  Ohkusu M, Raclavsky V, Takeo K. 2004. Induced synchrony in *Cryptococcus*

854    *neoformans* after release from $G_2$-arrest. *Antonie Van Leeuwenhoek* 85:37–44.

855  47.  Arora S, Hernandez Y, Erb-Downward JR, McDonald RA, Toews GB, Huffnagle

856    GB. 2005. Role of IFN-gamma in regulating $T_2$ immunity and the development of

857    alternatively activated macrophages during allergic bronchopulmonary mycosis. *J*

858    *Immunol* 174:6346–6356.

859    48.    Hardison SE, Ravi S, Wozniak KL, Young ML, Olszewski MA, Wormley FL. 2010.

860    Pulmonary infection with an interferon-gamma-producing *Cryptococcus*

861    *neoformans* strain results in classical macrophage activation and protection. *Am J*

862    *Pathol* 176:774–785.

863    49.    Leopold Wager CM, Wormley FL. 2014. Classical versus alternative macrophage

864    activation: the Ying and the Yang in host defense against pulmonary fungal

865    infections. *Mucosal Immunol* 7:1023–1035.

866    50.    Walachowski S, Tabouret G, Fabre M, Foucras G. 2017. Molecular analysis of a

867    short-term model of β-glucans-trained immunity highlights the accessory

868    contribution of GM-CSF in priming mouse macrophages response. *Front Immunol*

869    8:1089.

870    51.    Williment JA, Lin HH, Reid DM, Taylor PR, Williams DL, Wong SYC, Gordon S,

871    Brown GD. 2003. Dectin-1 expression and function are enhanced on alternatively

872    activated and GM-CSF-treated macrophages and are negatively regulated by IL-

873    10, dexamethasone, and lipopolysaccharide. *J Immunol* 171:4569–4573.

874    52.    Rosen LB, Freeman AF, Yang LM, Jutivorakool K, Olivier KN, Angkasekwinai N,

875    Suputtamongkol Y, Bennett JE, Pyrgos V, Williamson PR, Ding L, Holland SM,

876    Browne SK. 2013. Anti-GM-CSF autoantibodies in patients with cryptococcal

877    meningitis. *J Immunol* 190:3959–3966.

878    53.    Saijo T, Chen J, Chen SCA, Rosen LB, Yi J, Sorrell TC, Bennett JE, Holland SM,

879        Browne SK, Kwon-Chung KJ. 2014. Anti-granulocyte-macrophage colony-

880        stimulating factor autoantibodies are a risk factor for central nervous system

881        infection by *Cryptococcus gattii* in otherwise immunocompetent patients. *mBio*

882        5:e00912-14.

883   54.   Viola GM, Malek AE, Rosen LB, DiNardo AR, Nishiguchi T, Okhuysen PC,

884        Holland SM, Kontoyiannis DP. 2021. Disseminated cryptococcosis and anti-

885        granulocyte-macrophage colony-stimulating factor autoantibodies: an

886        underappreciated association. *Mycoses* 64:576–582.

887   55.   Altamirano S, Li Z, Fu MS, Ding M, Fulton SR, Yoder JM, Tran V, Nielsen K.

888        2021. The cyclin Cln1 controls polyploid Titan cell formation following a stress-

889        induced $G_2$ arrest in *Cryptococcus*. *mBio* 12:e0250921.

890   56.   Latil M, Rocheteau P, Châtre L, Sanulli S, Mémet S, Ricchetti M, Tajbakhsh S,

891        Chrétien F. 2012. Skeletal muscle stem cells adopt a dormant cell state post

892        mortem and retain regenerative capacity. *Nat Commun* 3:903.

893   57.   Kinoshita M, Johnson DL, Shatney CH, Lee YL, Mochizuki H. 2001. Cancer cells

894        surviving hypoxia obtain hypoxia resistance and maintain anti-apoptotic potential

895        under reoxygenation. *Int J Cancer* 91:322–326.

896   58.   Bagchi G, Das TK, Tyagi JS. Molecular analysis of the dormancy response in

897        *Mycobacterium smegmatis*: expression analysis of genes encoding the DevR-

898        DevS two-component system, Rv3134c and chaperone alpha-crystallin

899        homologues. *FEMS Microbiol Lett* 211:231–237.

900   59.   Qualls JE, Murray PJ. 2016. Immunometabolism within the tuberculosis

901        granuloma: amino acids, hypoxia, and cellular respiration. *Semin Immunopathol*

902    38:139–152.

903    60.    Alanio A. 2020. Dormancy in *Cryptococcus neoformans*: 60 years of accumulating

904           evidence. *J Clin Invest* 130:3353–3360.

905    61.    Cramer RA, Kowalski CH. 2021. Is it time to kill the survival curve? A case for

906           disease progression factors in microbial pathogenesis and host defense research.

907           *mBio* 12:e03483-20.

908    62.    Shibuya K, Coulson WF, Naoe S. 2002. Histopathology of deep-seated fungal

909           infections and detailed examination of granulomatous response against

910           cryptococci in patients with acquired immunodeficiency syndrome. *Nihon Ishinkin*

911           *Gakkai Zasshi* 43:143–151.

912    63.    O'Meara TR, Holmer SM, Selvig K, Dietrich F, Alspaugh JA. 2013. *Cryptococcus*

913           *neoformans* Rim101 Is associated with cell wall remodeling and evasion of the

914           host immune responses. *mBio* 4:e00522-12.

915

916    **FIGURE LEGENDS**

917    **Figure 1. Pulmonary granuloma formation in murine cryptococcal infections.** A.

918    Lung dissections of female C57BL/6 mice infected with the *mar1Δ* mutant strain were

919    performed to display macroscopic lung pathology, specifically granulomas (white

920    arrowheads). Cartoon adapted from BioRender.com (2021). B. The lungs of female

921    C57BL/6 mice inoculated with 1 x $10^4$ cells of the WT strain or the *mar1Δ* mutant strain

922    sacrificed at predetermined endpoints (3, 7, 14, and 40 DPI) were harvested for

923    histopathological analyses. Hematoxylin and eosin staining were utilized to visualize

924    microscopic lung pathology (fungal cells [yellow arrowheads], multinucleated giant cells

925 [yellow circle], epithelioid macrophages (yellow arrows), inset [yellow boxes]). 5x scale

926 bar (left), 250 μm. 10x scale bar (right), 50 μm. C. Granuloma diameter (μm) was

927 measured using FIJI. σ, standard deviation (μm). Gray box, no experimental subjects

928 can be assessed at this timepoint.

929

930 **Figure 2. Fungal burden throughout infection.** Pulmonary fungal burden of female

931 C57BL/6 mice ($n$ = 15) inoculated with 1 x $10^4$ cells of the WT strain or the *mar1Δ*

932 mutant strain was measured by quantitative cultures throughout infection: 3, 7, 14, and

933 21 DPI. Brain fungal burden of female C57BL/6 mice ($n$ = 15) inoculated with 1 x $10^4$

934 cells of the WT strain or the *mar1Δ* mutant strain was measured by quantitative cultures

935 at 21 DPI. Error bars represent standard error of the mean (SEM). Statistical

936 significance was determined using Student's $t$ test (***, $P$ < 0.001; ****, $P$ < 0.0001; ns,

937 not significant).

938

939 **Figure 3. Pulmonary cytokine profile and leukocyte infiltrate associated with**

940 **granuloma formation.** A. Pulmonary cytokine responses of female C57BL/6 mice

941 inoculated with 1 x $10^4$ cells of the WT strain or the *mar1Δ* mutant strain were measured

942 using the Bio-Plex protein array system throughout infection: 1 ($n$ = 15), 3 ($n$ = 15), 7 ($n$

943 = 10), 14 ($n$ = 10), and 21 ($n$ = 10) DPI. Error bars represent SEM. Statistical

944 significance between strains at each timepoint was determined using Student's $t$ test (*,

945 $P$ < 0.05; **, $P$ < 0.01; ***, $P$ < 0.001; ****, $P$ < 0.0001; no designation between strains,

946 not significant). Only a subset of data is shown; refer to Figure S2 for full analysis. B.

947 Pulmonary leukocyte infiltrates of female C57BL/6 mice inoculated with 1 x $10^4$ cells of

948   the WT strain or the *mar1Δ* mutant strain were measured by flow cytometry throughout

949   infection: 1, 3, 7, and 21 DPI. Data shown are the mean ± of absolute cell numbers from

950   three independent experiments (*n* = 3) performed using five mice per group per

951   timepoint per experiment. Error bars represent SEM. Statistical significance between

952   strains at each timepoint was determined using Student's *t* test (*, *P* < 0.05; no

953   designation between strains, not significant). Only a subset of data is shown; refer to

954   Figure S3 for full analysis. C. Pulmonary macrophage activation of female C57BL/6

955   mice (*n* = 3) inoculated with 1 x 10$^4$ cells of the WT strain or the *mar1Δ* mutant strain

956   were measured by flow cytometry throughout infection: 7, 14, and 21 DPI. Inducible

957   nitrogen oxide synthase (iNOS) was used as a marker for M1 macrophages and

958   Arginase 1 (Arg1) was used as a marker for M2 macrophages. The percentage of total

959   iNOS+ cells and Arg1+ cells is shown. Error bars represent the SEM. Log

960   transformation was used to normally distribute the data for statistical analysis. Statistical

961   significance between strains at each timepoint was determined using Student's *t* test (*,

962   *P* < 0.05; no designation between strains, not significant). AM = alveolar macrophage

963   (CD45+, CD11b-). IM = interstitial macrophage (CD45+, CD11b+). Cartoons adapted

964   from BioRender.com (2021).

965

966   **Figure 4. Contributions of GM-CSF signaling to pulmonary granuloma formation.**

967   A. The lungs of female (*n* = 2) (shown) and male (*n* = 2) (not shown) Csf2rb$^{-/-}$ mice

968   inoculated with 1 x 10$^4$ cells of the WT strain or the *mar1Δ* mutant strain sacrificed at

969   predetermined endpoints (3, 7, and 14 DPI) were harvested for histopathological

970   analyses. Hematoxylin and eosin staining were utilized to visualize microscopic lung

43

971    pathology (fungal cells [yellow arrowheads], inset [yellow boxes]). 5x scale bar (left),

972    250 $\mu$m. 10x scale bar (right), 50 $\mu$m.  B. Pulmonary fungal burden of female ($n$ = 2) and

973    male ($n$ = 2) Csf2rb$^{-/-}$ mice inoculated with 1 x 10$^4$ cells of the WT strain or the $mar1\Delta$

974    mutant strain sacrificed at 3 DPI was measured by quantitative cultures. Error bars

975    represent the SEM. Statistical significance was determined using Student's $t$ test (*, $P <$

976    0.05).

977

978    **Figure 5. Cell cycle-mediated virulence factor phenotypes of the $mar1\Delta$ mutant**

979    **strain.** A. Titan cell formation was induced in the WT strain, the $mar1\Delta$ mutant strain,

980    and the $mar1\Delta$ + $MAR1$ complemented strain. Cells were pre-grown in YNB medium at

981    30°C and an OD$_{600}$ of 0.001 was transferred to 10% HI-FBS in PBS incubated at 5%

982    CO$_2$, 37°C for 96 hours. Cells were imaged by DIC microscopy (Zeiss Axio Imager A1).

983    Cell diameter was measured using FIJI, and cells with a diameter > 10 µm were

984    considered Titan cells (red arrowheads). The number of Titan cells per 10,000 cells was

985    calculated for each strain. A minimum of 400 cells were analyzed across three biological

986    replicates ($n$ = 3). Error bars represent the SEM. Statistical significance was determined

987    using a one-way ANOVA (*, $P$ < 0.05; ns, not significant). 63x scale bar, 10 $\mu$m. B. The

988    WT strain, the $mar1\Delta$ mutant strain, the $mar1\Delta$ + $MAR1$ complemented strain, and the

989    $cap59\Delta$ mutant strain were incubated in YPD medium at 30°C and CO$_2$-independent

990    medium (TC) at 37°C until saturation. Samples were subsequently fixed, mounted,

991    dehydrated, and sputter-coated. Samples were imaged with a Hitachi S-4700 scanning

992    electron microscope to visualize capsule organization and elaboration.

993

44

994 **Figure 6. Slow growth phenotypes of the *mar1Δ* mutant strain.** A. Morphological

995 defects were analyzed in the WT strain, the *mar1Δ* mutant strain, and the *mar1Δ +*

996 *MAR1* complemented strain through incubation in YPD medium at either 30°C or 37°C.

997 Cells were imaged by DIC microscopy (Zeiss Axio Imager A1) and were subsequently

998 visually inspected for morphological defects, such as elongated cells (red squares),

999 wide bud necks (red arrowhead), and cytokinesis failure (red circle). The percentage of

1000 total cells displaying morphological defects was quantified for each strain at each

1001 temperature. A minimum of 500 cells were analyzed across three biological replicates

1002 ($n = 3$). Error bars represent the SEM. Log transformation was used to normally

1003 distribute the data for statistical analysis (two-way ANOVA; *, $P < 0.05$; **, $P < 0.01$; ns,

1004 not significant). 63x scale bar, 10 $\mu$m. B. Growth of the WT strain, the *mar1Δ* mutant

1005 strain, and the *mar1Δ + MAR1* complemented strain was assessed in YPD medium at

1006 37°C. Growth was tracked for 40 hours and was measured by absorbance at $OD_{600}$.

1007 Figure summarizes data across three biological replicates ($n = 3$). Error bars represent

1008 the SEM. C. Hypoxia resistance was assessed by growth on YES medium in the

1009 presence of $CoCl_2$ (0.7 mM) and in a microaerophilic chamber. Serial dilutions of the WT

1010 strain, the *mar1Δ* mutant strain, the *mar1Δ + MAR1* complemented strain, and the *sre1Δ*

1011 mutant strain were spotted onto agar plates and incubated at 30°C. Results were

1012 compared to the same strains grown in ambient air conditions.

1013

1014 **Table 1. Fungal strains used in this study.**

| Strain | Genotype | Source |
|--------|----------|--------|
| H99 | *MATα* | (13) |
| MAK1 | *MATα mar1Δ::NAT* | (23) |

45

| MAK11 | *MATα mar1Δ::NAT + MAR1-NEO* | (23) |
| cap59 | *MATα cap59Δ::NEO* | (63) |
| HEB6 | *MATα sre1Δ::NEO* | (31) |

1015

1016 **Figure S1. Additional histopathology granuloma images.** A. Medium power image

1017 from a WT-infected C57BL/6 mouse at 7 DPI, demonstrating a moderate peribronchiolar

1018 neutrophilic and mononuclear inflammatory reaction with vague, early, and poorly

1019 formed granulomata formation (10X). B. Low power image from a *mar1Δ*-infected

1020 C57BL/6 mouse at 3 DPI, demonstrating an absence of a significant inflammatory

1021 reaction (4X). C, D. Low power image (C) from a *mar1Δ*-infected C57BL/6 mouse at 40

1022 DPI showing a relatively well-circumscribed nodule containing well developed

1023 organizing lymphohistiocytic inflammation and medium power view (D) highlighting

1024 compact histiocytic aggregates and peripheral mononuclear cells, characteristic of

1025 granuloma formation (C; 4X, D; 10X). E. Medium power image from a WT-infected

1026 Csf2rb$^{-/-}$ mouse at 7 DPI showing a marked peribronchiolar neutrophilic and

1027 mononuclear inflammatory reaction without granuloma formation (10X). F. Low power

1028 image from a WT-infected Csf2rb$^{-/-}$ mouse at 14 DPI demonstrating an absence of a

1029 significant inflammatory reaction (4X). All images are of hematoxylin- and eosin-stained

1030 tissue sections.

1031

1032 **Figure S2. Complete pulmonary cytokine profile throughout infection.** Pulmonary

1033 cytokine responses of female C57BL/6 mice inoculated with 1 x 10$^4$ cells of the WT

1034 strain or the *mar1Δ* mutant strain were measured using the Bio-Plex protein array

1035 system throughout infection: 1 (*n* = 15), 3 (*n* = 15), 7 (*n* = 10), 14 (*n* = 10), and 21 (*n* =

46

1036    10) DPI. Error bars represent SEM. Statistical significance between strains at each

1037    timepoint was determined using Student's *t* test (*, *P* < 0.05; **, *P* < 0.01; ***, *P* < 0.001;

1038    ****, *P* < 0.0001; no designation between strains, not significant).

1039

1040    **Figure S3. Complete pulmonary leukocyte infiltrate response throughout**

1041    **infection.** Pulmonary immune cell infiltrates of female C57BL/6 mice inoculated with 1 x

1042    $10^4$ cells of the WT strain or the *mar1Δ* mutant strain were measured by flow cytometry

1043    throughout infection: 1, 3, 7, 14, and 21 DPI. Data shown are the mean ± of absolute

1044    cell numbers from three independent experiments (*n* = 3) performed using five mice per

1045    group per timepoint per experiment. Error bars represent the SEM. Statistical

1046    significance between strains at each timepoint was determined using Student's *t* test (*,

1047    *P* < 0.05; **, *P* < 0.01; no designation between strains, not significant).

1048

1049    **Figure S4. Recovery of *mar1Δ* mutant cells from murine lungs at extended**

1050    **timepoints in infection.** Lungs from female C57BL/6 mice infected with the *mar1Δ*

1051    mutant strain were harvested at 61 and 100 DPI. Single fungal colonies were isolated

1052    on YPD agar plates and subsequently incubated in various conditions that allowed for

1053    identification of *mar1Δ* mutant isolates: YPD medium at 30°C, YPD medium at 37°C,

1054    YPD medium + nourseothricin (NAT), and YPD medium pH 8.15. The original WT strain

1055    (A1) and *mar1Δ* mutant strain (A2) are included as controls in each condition.

1056

1057    **Figure S5. Granuloma formation and maintenance timeline.** Chronological summary

1058    of important observations about granuloma formation and maintenance in the WT strain

47

1059    (top) and *mar1Δ* mutant strain (bottom) backgrounds. Cartoons adapted from
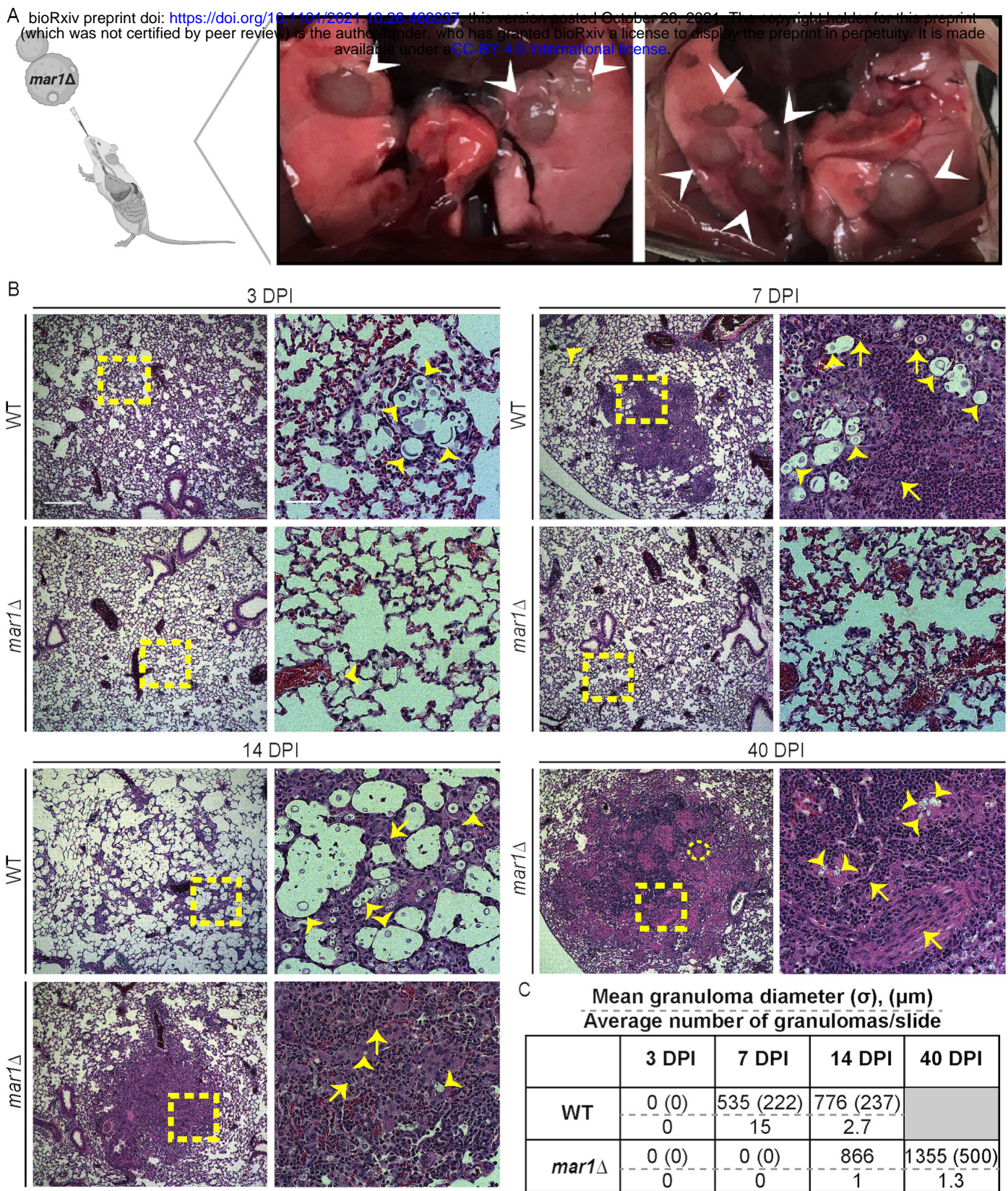
1060    BioRender.com (2021).

## Mean granuloma diameter (σ), (μm)
### Average number of granulomas/slide

| | 3 DPI | 7 DPI | 14 DPI | 40 DPI |
|---|---|---|---|---|
| **WT** | 0 (0)<br>0 | 535 (222)<br>15 | 776 (237)<br>2.7 | |
| ***mar1Δ*** | 0 (0)<br>0 | 0 (0)<br>0 | 866<br>1 | 1355 (500)<br>1.3 |

**Figure 1. Pulmonary granuloma formation in murine cryptococcal infections.** A. Lung dissections of female C57BL/6 mice infected with the *mar1Δ* mutant strain were performed to display macroscopic lung pathology, specifically granulomas (white arrowheads). Cartoon adapted from BioRender.com (2021). B. The lungs of female C57BL/6 mice inoculated with 1 x 10⁴ cells of the WT strain or the *mar1Δ* mutant strain sacrificed at predetermined endpoints (3, 7, 14, and 40 DPI) were harvested for histopathological analyses. Hematoxylin and eosin staining were utilized to visualize microscopic lung pathology (fungal cells [yellow arrowheads], multinucleated giant cells [yellow circle], epithelioid macrophages (yellow arrows), inset [yellow boxes]). 5x scale bar (left), 250 μm. 10x scale bar (right), 50 μm. C. Granuloma diameter (μm) was measured using FIJI. σ, standard deviation (μm). Gray box, no experimental subjects can be assessed at this timepoint.
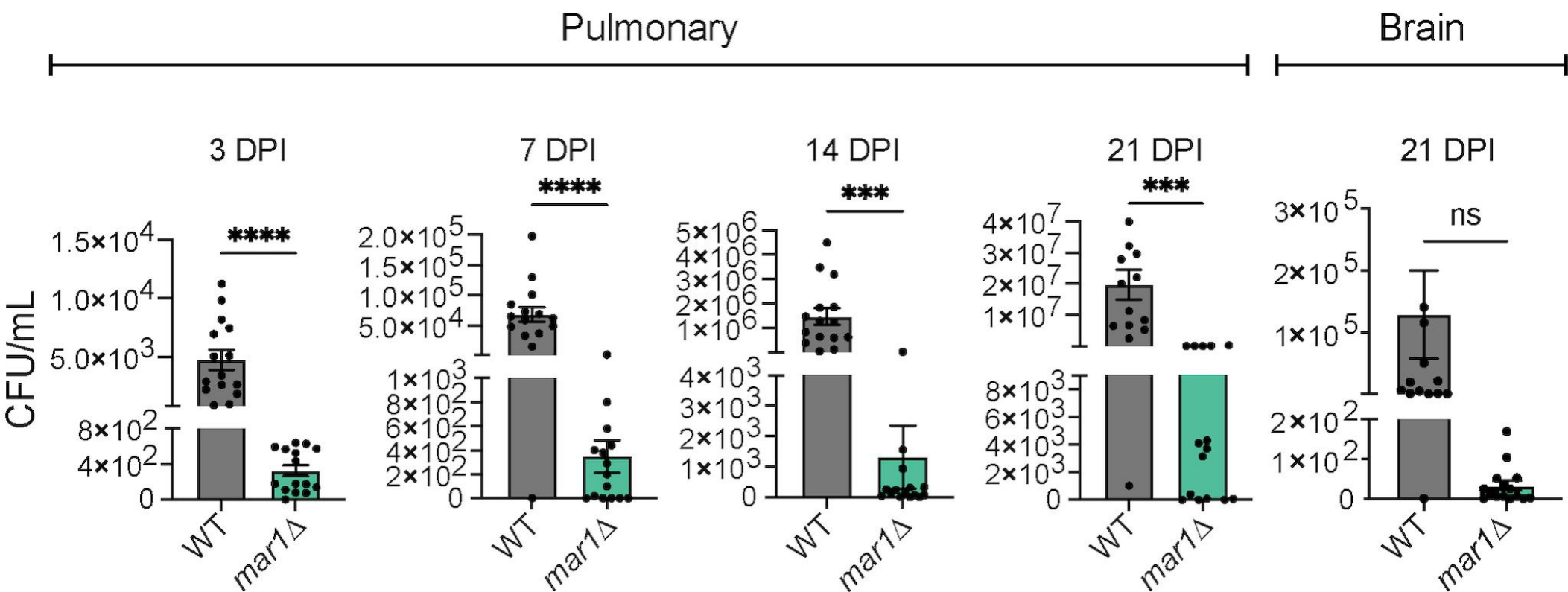
**Figure 2. Fungal burden throughout infection.** Pulmonary fungal burden of female C57BL/6 mice ($n$ = 15) inoculated with 1 x $10^4$ cells of the WT strain or the *mar1Δ* mutant strain was measured by quantitative cultures throughout infection: 3, 7, 14, and 21 DPI. Brain fungal burden of female C57BL/6 mice ($n$ = 15) inoculated with 1 x $10^4$ cells of the WT strain or the *mar1Δ* mutant strain was measured by quantitative cultures at 21 DPI. Error bars represent standard error of the mean (SEM). Statistical significance was determined using Student's $t$ test (***, $P < 0.001$; ****, $P < 0.0001$; ns, not significant).
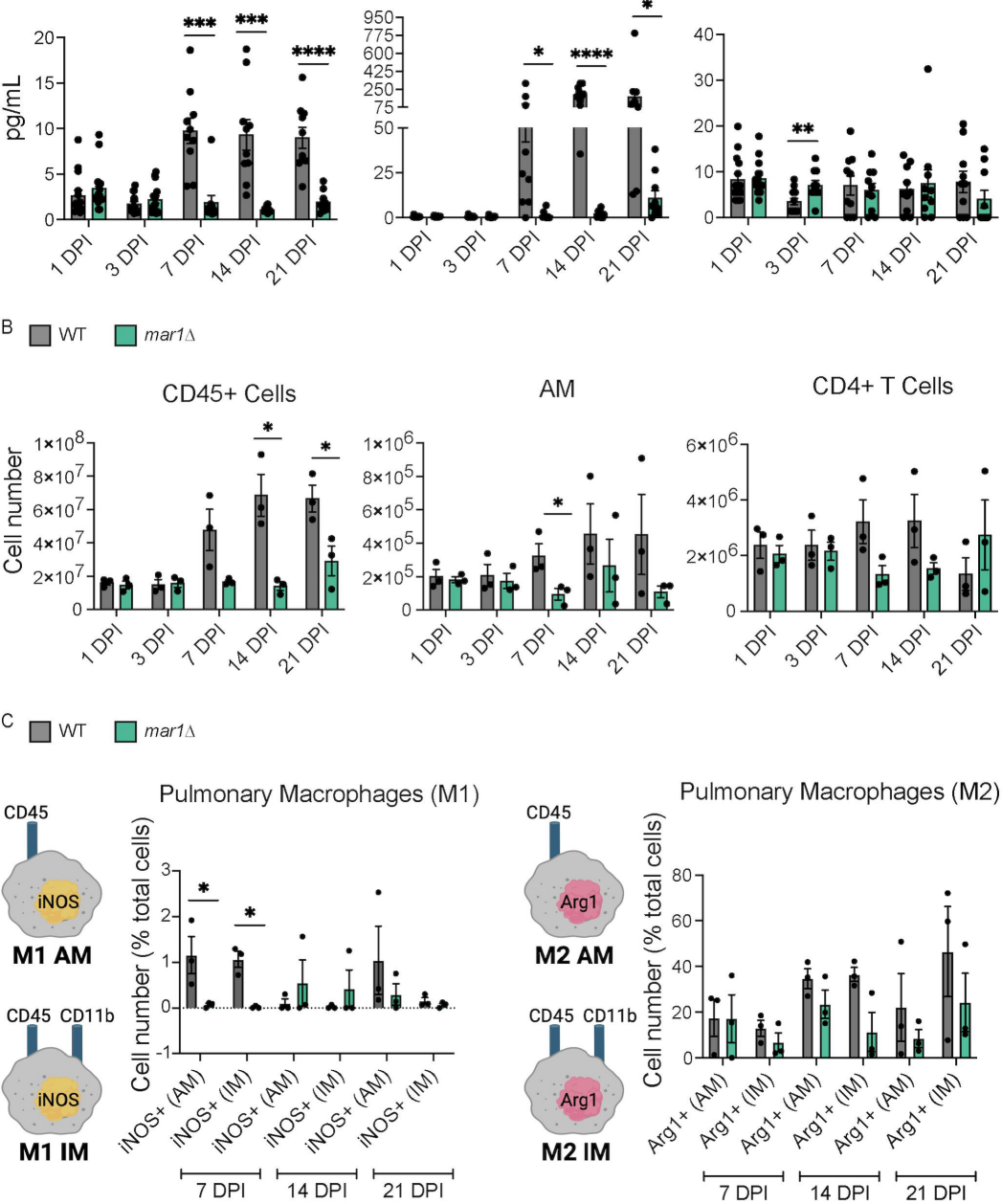
**Figure 3. Pulmonary cytokine profile and leukocyte infiltrate associated with granuloma formation.** A. Pulmonary cytokine responses of female C57BL/6 mice inoculated with 1 x 10$^4$ cells of the WT strain or the *mar1Δ* mutant strain were measured using the Bio-Plex protein array system throughout infection: 1 (*n* = 15), 3 (*n* = 15), 7 (*n* = 10), 14 (*n* = 10), and 21 (*n* = 10) DPI. Error bars represent SEM. Statistical significance between strains at each timepoint was determined using Student's *t* test (*, *P* < 0.05; **, *P* < 0.01; ***, *P* < 0.001; ****, *P* < 0.0001; no designation between strains, not significant). Only a subset of data is shown; refer to Figure S2 for full analysis. B. Pulmonary leukocyte infiltrates of female C57BL/6 mice inoculated with 1 x 10$^4$ cells of the WT strain or the *mar1Δ* mutant strain were measured by flow cytometry throughout infection: 1, 3, 7, and 21 DPI. Data shown are the mean ± of absolute cell numbers from three independent experiments (*n* = 3) performed using five mice per group per timepoint per experiment. Error bars represent SEM. Statistical significance between strains at each timepoint was determined using Student's *t* test (*, *P* < 0.05; no designation between strains, not significant). Only a subset of data is shown; refer to Figure S3 for full analysis. C. Pulmonary macrophage activation of female C57BL/6 mice (*n* = 3) inoculated with 1 x 10$^4$ cells of the WT strain or the *mar1Δ* mutant strain were measured by flow cytometry throughout infection: 7, 14, and 21 DPI. Inducible nitrogen oxide synthase (iNOS) was used as a marker for M1 macrophages and Arginase 1 (Arg1) was used as a marker for M2 macrophages. The percentage of total iNOS+ cells and Arg1+ cells is shown. Error bars represent the SEM. Log transformation was used to normally distribute the data for statistical analysis. Statistical significance between strains at each timepoint was determined using Student's *t* test (*, *P* < 0.05; no designation between strains, not significant). AM = alveolar macrophage (CD45+, CD11b-). IM = interstitial macrophage (CD45+, CD11b+). Cartoons adapted from BioRender.com (2021).
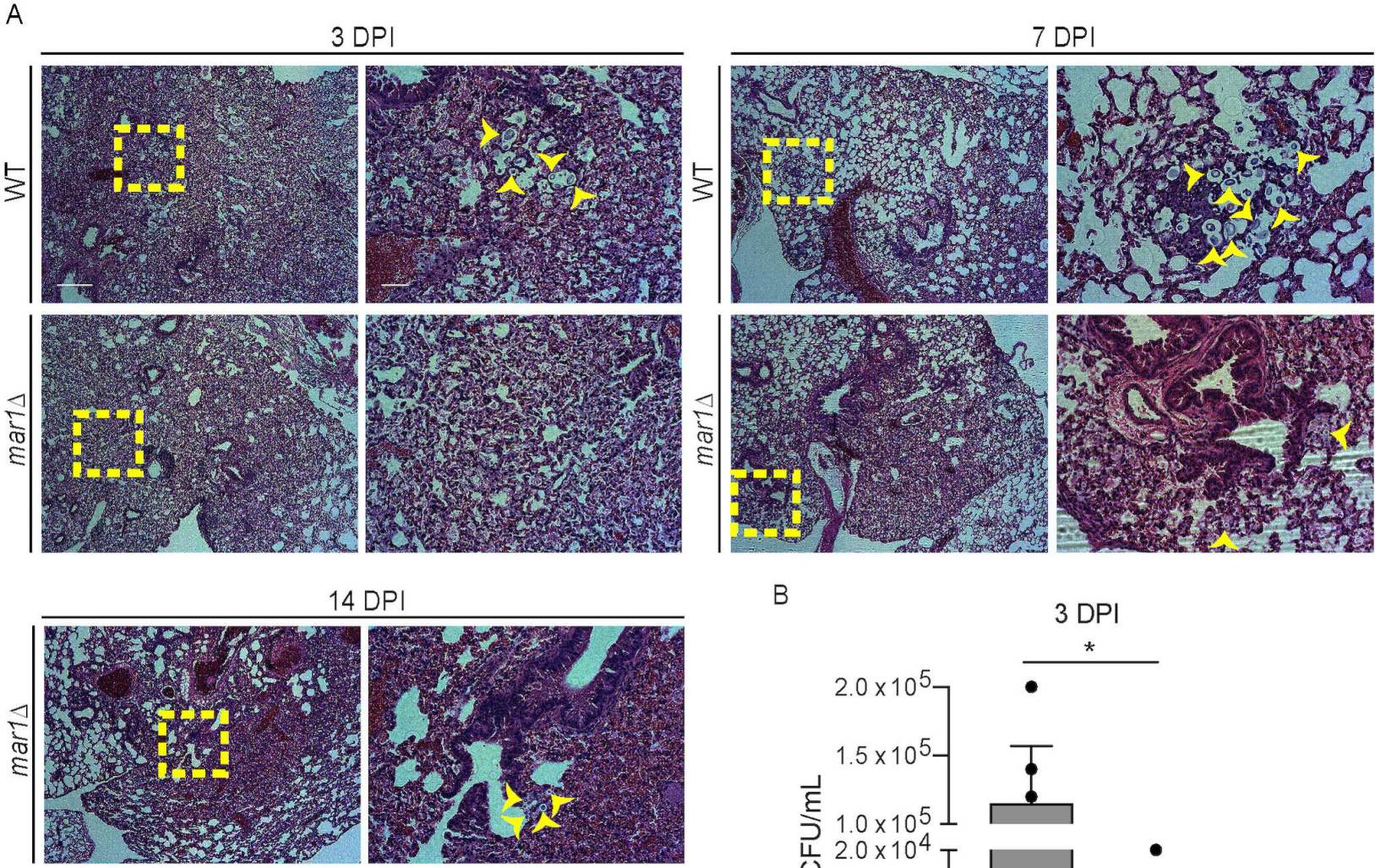
**Figure 4. Contributions of GM-CSF signaling to pulmonary granuloma formation.**
A. The lungs of female ($n$ = 2) (shown) and male ($n$ = 2) (not shown) Csf2rb$^{-/-}$ mice inoculated with 1 x 10$^4$ cells of the WT strain or the *mar1Δ* mutant strain sacrificed at predetermined endpoints (3, 7, and 14 DPI) were harvested for histopathological analyses. Hematoxylin and eosin staining were utilized to visualize microscopic lung pathology (fungal cells [yellow arrowheads], inset [yellow boxes]). 5x scale bar (left), 250 μm. 10x scale bar (right), 50 μm.  B. Pulmonary fungal burden of female ($n$ = 2) and male ($n$ = 2) Csf2rb$^{-/-}$ mice inoculated with 1 x 10$^4$ cells of the WT strain or the *mar1Δ* mutant strain sacrificed at 3 DPI was measured by quantitative cultures. Error bars represent the SEM. Statistical significance was determined using Student's *t* test (*, $P$ < 0.05).
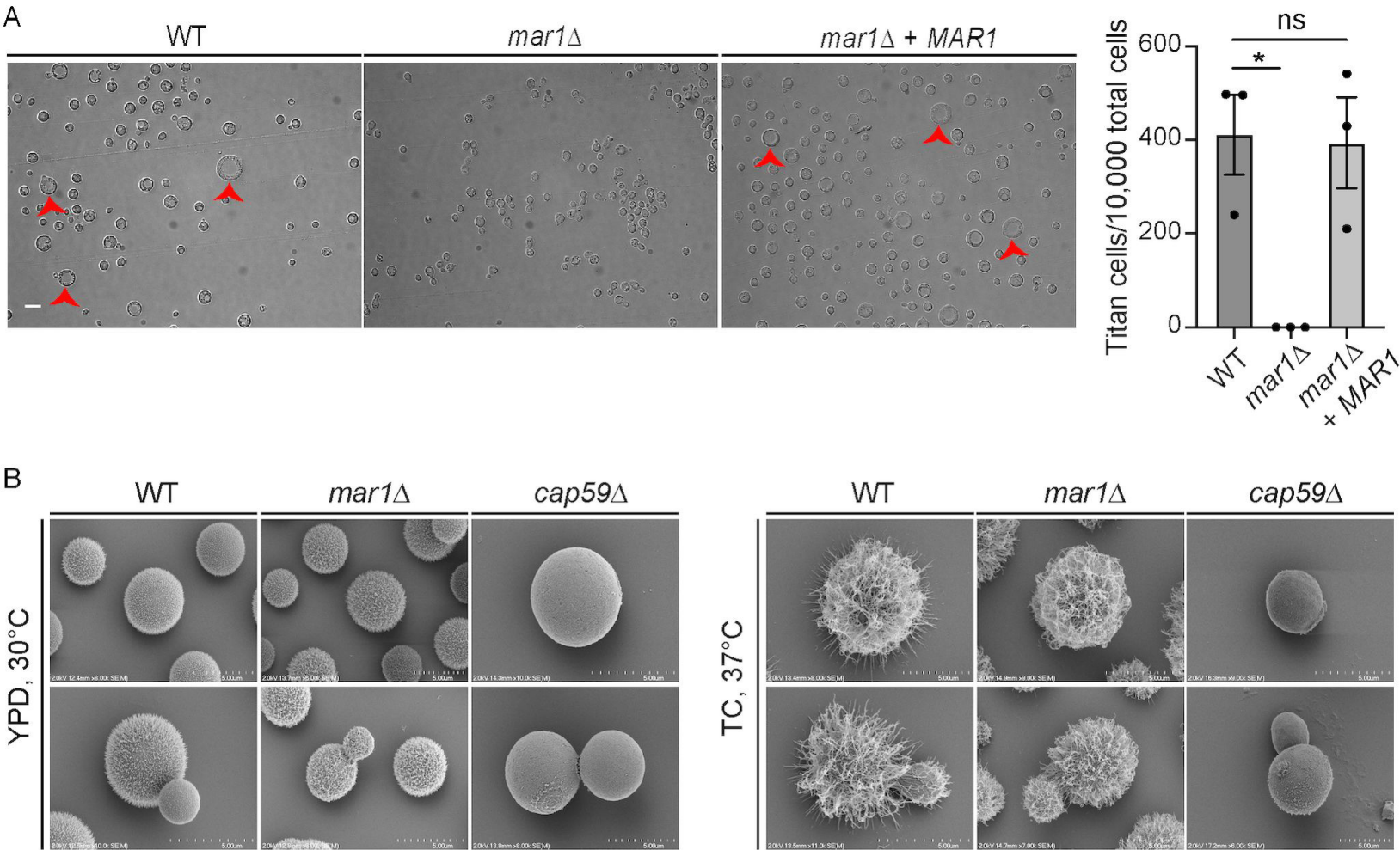
**Figure 5. Cell cycle-mediated virulence factor phenotypes of the *mar1Δ* mutant strain.**
A. Titan cell formation was induced in the WT strain, the *mar1Δ* mutant strain, and the *mar1Δ* + *MAR1* complemented strain. Cells were pre-grown in YNB medium at 30°C and an $OD_{600}$ of 0.001 was transferred to 10% HI-FBS in PBS incubated at 5% $CO_2$, 37°C for 96 hours. Cells were imaged by DIC microscopy (Zeiss Axio Imager A1). Cell diameter was measured using FIJI, and cells with a diameter > 10 μm were considered Titan cells (red arrowheads). The number of Titan cells per 10,000 cells was calculated for each strain. A minimum of 400 cells were analyzed across three biological replicates (*n* = 3). Error bars represent the SEM. Statistical significance was determined using a one-way ANOVA (*, $P < 0.05$; ns, not significant). 63x scale bar, 10 μm. B. The WT strain, the *mar1Δ* mutant strain, the *mar1Δ* + *MAR1* complemented strain, and the *cap59Δ* mutant strain were incubated in YPD medium at 30°C and $CO_2$-independent medium (TC) at 37°C until saturation. Samples were subsequently fixed, mounted, dehydrated, and sputter-coated. Samples were imaged with a Hitachi S-4700 scanning electron microscope to visualize capsule organization and elaboration.
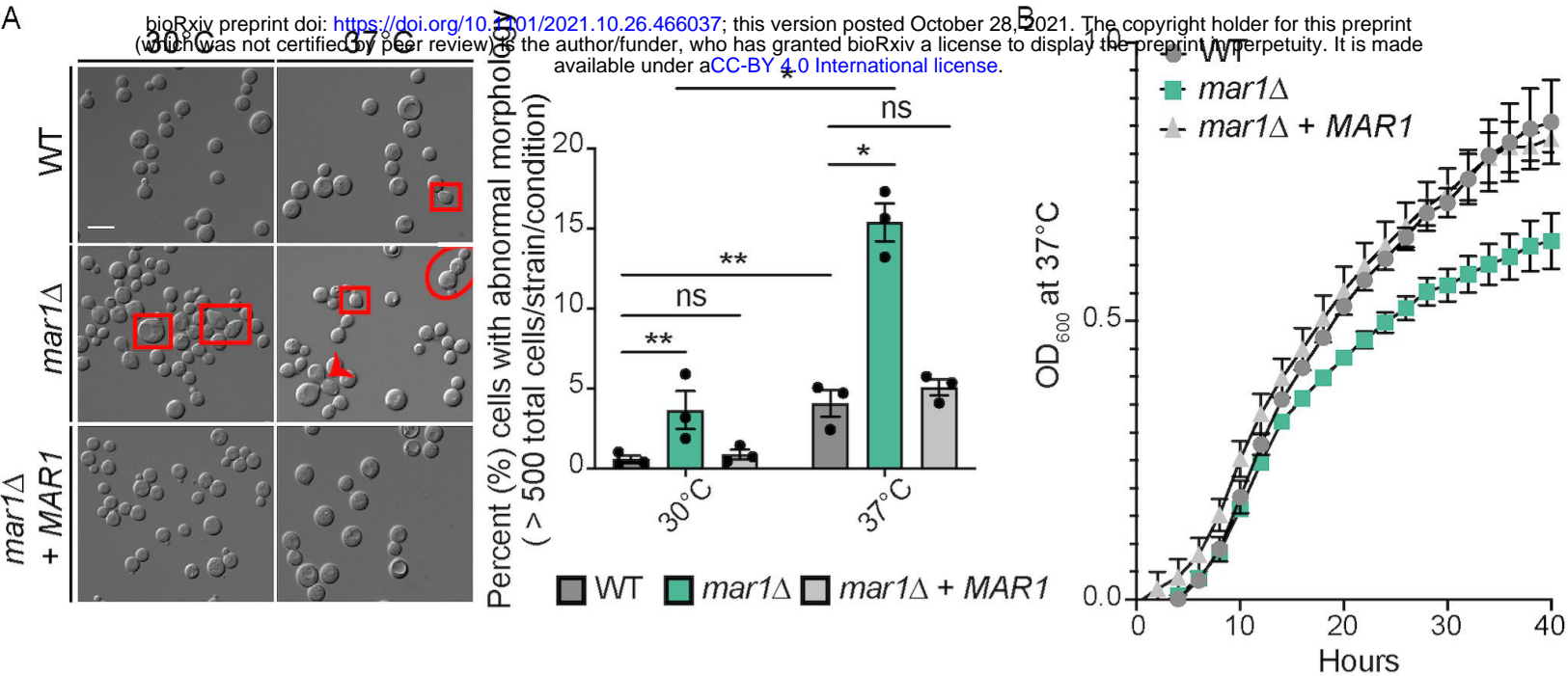
**Figure 6. Slow growth phenotypes of the *mar1Δ* mutant strain.** A. Morphological defects were analyzed in the WT strain, the *mar1Δ* mutant strain, and the *mar1Δ* + *MAR1* complemented strain through incubation in YPD medium at either 30°C or 37°C. Cells were imaged by DIC microscopy (Zeiss Axio Imager A1) and were subsequently visually inspected for morphological defects, such as elongated cells (red squares), wide bud necks (red arrowhead), and cytokinesis failure (red circle). The percentage of total cells displaying morphological defects was quantified for each strain at each temperature. A minimum of 500 cells were analyzed across three biological replicates (*n* = 3). Error bars represent the SEM. Log transformation was used to normally distribute the data for statistical analysis (two-way ANOVA; *, $P < 0.05$; **, $P < 0.01$; ns, not significant). 63x scale bar, 10 μm. B. Growth of the WT strain, the *mar1Δ* mutant strain, and the *mar1Δ* + *MAR1* complemented strain was assessed in YPD medium at 37°C. Growth was tracked for 40 hours and was measured by absorbance at $OD_{600}$. Figure summarizes data across three biological replicates (*n* = 3). Error bars represent the SEM. C. Hypoxia resistance was assessed by growth on YES medium in the presence of $CoCl_2$ (0.7 mM) and in a microaerophilic chamber. Serial dilutions of the WT strain, the *mar1Δ* mutant strain, the *mar1Δ* + *MAR1* complemented strain, and the *sre1Δ* mutant strain were spotted onto agar plates and incubated at 30°C. Results were compared to the same strains grown in ambient air conditions.